

Document downloaded from the institutional repository of the University of Alcalá: <http://ebuah.uah.es/dspace/>

This is a postprint version of the following published document:

Belenguer-Plomer, M.A. et al. (2019) 'Burned area detection and mapping using Sentinel-1 backscatter coefficient and thermal anomalies', *Remote sensing of environment*, 233, p. 111345.

Available at <http://dx.doi.org/10.1016/j.rse.2019.111345>

© 2019 Elsevier

(Article begins on next page)



This work is licensed under a

Creative Commons Attribution-NonCommercial-NoDerivatives
4.0 International License.

Burned area detection and mapping using Sentinel-1 backscatter coefficient and thermal anomalies

Miguel A. Belenguer-Plomer^{a,*}, Mihai A. Tanase^{a,b}, Angel Fernandez-Carrillo^a, Emilio Chuvieco^a

^a*Environmental Remote Sensing Research Group, Dep. of Geology, Geography and Environment, Universidad de Alcalá, Colegios 2, Alcalá de Henares 28801, Spain*

^b*School of Ecosystem and Forest Sciences, University of Melbourne, Parkville 3052, Australia*

Abstract

This paper presents a burned area mapping algorithm based on change detection of Sentinel-1 backscatter data guided by thermal anomalies. The algorithm self-adapts to the local scattering conditions and it is robust to variations of input data availability. The algorithm applies the Reed-Xiaoli detector (RXD) to distinguish anomalous changes of the backscatter coefficient. Such changes are linked to fire events, which are derived from thermal anomalies (hotspots) acquired during the detection period by the Moderate Resolution Imaging Spectroradiometer (MODIS) and the Visible Infrared Imaging Radiometer Suite (VIIRS) sensors. Land cover maps were used to account for changing backscatter behaviour as the RXD is class dependent. A machine learning classifier (random forests) was used to detect burned areas where hotspots were not available. Burned area perimeters derived from optical images (Landsat-8 and Sentinel-2) were used to validate the algorithm results. The validation dataset covers 21 million hectares in 18 locations that represent the main biomes affected by fires, from boreal forests to tropical and sub-tropical forests and savannas. A mean Dice coefficient (DC) over all studied locations of 0.59 ± 0.06 (\pm confidence interval, 95%) was obtained. Mean omission (OE) and commission errors (CE) were 0.43 ± 0.08 and 0.37 ± 0.06 , respectively. Comparing results with the MODIS based MCD64A1 Version 6, our detections are quite promising, improving on average DC by 0.13 and reducing OE and CE by 0.12 and 0.06, respectively.

Keywords: Burned area detection, Sentinel-1, backscatter coefficient, SAR, Random forests, Reed-Xiaoli detector, Fire

1. Introduction

Fire is one of the natural agents that most alter terrestrial ecosystems and has a key ecological role in a large part of the Earth's surface. Fires may have local to global effects as they reduce soil fertility, change water supply, increase biodiversity loss and negatively influence carbon sequestration (Hoffmann et al., 2002; Van der Werf et al., 2010; Hansen et al., 2013; Bond et al., 2005; Aponte et al., 2016; Pausas & Paula, 2012; Lavorel et al., 2007). Fires may

*Corresponding author

Email address: miguel.belenguer@uah.es (Miguel A. Belenguer-Plomer)

29 also alter global biochemical cycles by modifying the emitted greenhouse gases (GHGs) and aerosols presence in the
30 atmosphere (Van Der Werf et al., 2017; Andreae & Merlet, 2001; Bowman et al., 2009). Annual global estimates of
31 carbon emissions from forest fires are quite variable. Van der Werf et al. (2010) place them between 1.6 and 2.8 PgC
32 per year, which is equivalent to 20 to 30% of the global carbon emissions generated by burning fossil fuels (Kloster
33 et al., 2012; Flannigan et al., 2009). However, other authors estimate fire related emissions at 2 to 4 PgC per year, the
34 equivalent of up to 50% of fossil fuel emissions (Bowman et al., 2009). Regardless of the actual value, changes in
35 global burned area (BA) remains an important source of interannual variability of atmospheric carbon concentration.
36 Direct relationships between global warming and the frequency of fires at the global level implies a positive feedback
37 process with sufficient potential to be a key factor in climate change (Flannigan et al., 2009; Hoffmann et al., 2002;
38 Knorr et al., 2016). Although the current understanding of all these interactions is limited (Krawchuk et al., 2009),
39 increased carbon concentration in the atmosphere may reinforce the effect of climate on fire frequency and intensity
40 (Langenfelds et al., 2002; Flannigan et al., 2006). Such increases are spatially variable. Furthermore, some areas may
41 not experience changes with respect to current fire regimes, while others may even experience reduced fire occurrence
42 (Flannigan et al., 2009; Kloster et al., 2012; Andela et al., 2017).

43 Given the relationship between the fire regime and climate, the Global Climate Observing System (GCOS) con-
44 siders fire disturbance as an Essential Climatic Variable (ECV). An ECV is a physical, chemical, biological or a group
45 of linked variables that contributes in a critical way to the characterization of the climate system, being key to study
46 and predict its evolution (Bojinski et al., 2014). The origin of ECVs dates back to the 1990s, when gaps in climate
47 knowledge and the reduction of observation networks in many countries led GCOS to develop the ECV concept to
48 simplify the study of climate through systematic observations of a limited set of variables with great climatic impor-
49 tance using satellite remote sensing data (Hollmann et al., 2013; Bradley et al., 2012). In 2010, the European Space
50 Agency (ESA) started the Climate Change Initiative (CCI) programme as the main contribution of the Agency to the
51 GCOS agenda. The CCI programme aims to obtain information on different ECVs using remote sensing data to help
52 improving climate modelling (Plummer et al., 2017; Hollmann et al., 2013). Fire Disturbance is one of the ECV in-
53 cluded in the first phase of the CCI programme initiated in 2010. The goals of this project were to produce long-term
54 and consistent time series of global BA information (Chuvieco et al., 2016). The interest of global BA products for
55 climate modelling has been reviewed by several authors (Mouillot et al., 2014; Poulter et al., 2015). And many global
56 BA products have been released over the last years (Humber et al., 2018). Three such products were based on data
57 from the NASA's Moderate Resolution Imaging Spectrometer (MODIS) sensor, the MCD45 (Roy et al., 2008), the
58 MCD64 (Giglio et al., 2009, 2018) and the MODIS Fire_cci v5.0 (Chuvieco et al., 2018). Images acquired by the
59 VEGETATION sensor on board the SPOT-4 (Satellite Pour Observation de la Terre) satellite have also been used to
60 generate global BA products, namely the Global Burnt Area (GBA) 2000 (Tansey et al., 2004), Globcarbon (Plummer
61 et al., 2006), L3JRC (Tansey et al., 2008) and the Copernicus Global Land Service Burnt Area (based on Proba-V
62 since 2014: land.copernicus.eu/global/products/ba). Furthermore, the European Remote Sensing Satellite - Advanced
63 Along Track Scanning Radiometer (ERS2-ATSR2) was used to generate the Globscar product (Simon et al., 2004)

64 while the MEdium Resolution Imaging Spectrometer (MERIS) data were used to generate the Fire_cci v4.1 product
65 (Alonso-Canas & Chuvieco, 2015; Chuvieco et al., 2016). All these products were obtained using passive remote
66 sensing datasets (optical and thermal wavelengths) which have significant limitations in areas with persistent cloud
67 cover. Another limitation comes from the relatively coarse (> 250 m) spatial resolutions of these sensors, which
68 makes the detection of small fires difficult (Stroppiana et al., 2015a; Randerson et al., 2012).

69 Several factors limit burned area mapping from remote sensing data. These factors are related to both, the sensor
70 characteristics and the observed scene. The type of sensor (passive or active) and the region of the electromagnetic
71 spectrum in which the images are acquired are decisive in the success of the burned area detection. Among the scene
72 characteristics influencing detection accuracy, the size and shape of fire patches, land cover type, fire unrelated changes
73 (e.g., phenology, floods, harvest, insects) and the presence of clouds (optical and thermal part of the spectrum) are the
74 most relevant. Since sensor and scene related factors interact, the degree to which each of the mentioned factors affect
75 BA detection success varies (Eva & Lambin, 1998; Boschetti et al., 2004; Belenguer-Plomer et al., 2018a; Padilla
76 et al., 2015). The spatial and temporal resolution of the sensor have a significant impact on BA mapping accuracy,
77 determining the minimum size of the fires that can be detected (Boschetti et al., 2004) and the time interval between
78 fire and detection (Eva & Lambin, 1998). However, previous studies suggest that temporal resolution is less important
79 than the spatial resolution when it comes to the accuracy of the BA detection (Boschetti et al., 2010).

80 In a survey based on a questionnaire of 47 researchers who used BA products and an extended literature review,
81 Mouillot et al. (2014) suggested that BA products should have commission errors (CE) in the range of 4% (ideal) to
82 17 % (maximum) while omission errors (OE) above 19% were deemed less useful for the climate modelling efforts.
83 A first global comparison analysis found that the NASA's MCD64 was the most accurate BA product (Padilla et al.,
84 2015), but was far from achieving these goals with CE and OE reaching 42% and respectively 68%. These errors
85 were in part due to the low spatial resolution which results in small fires being overlooked (Randerson et al., 2012). A
86 recent study has demonstrated that the contribution of small fires may be in fact even greater, as comparing Sentinel-2
87 and MODIS products for Africa showed an underestimation of almost 45% of BA (Roteta et al., 2019). Therefore, the
88 development of new BA detection algorithms is a relevant research topic in the current context where climate change
89 is a key issue. To achieve this improvement, the use of images from new satellites, such as those of the Copernicus
90 missions of ESA, is necessary. Furthermore, alternative mapping options (e.g., radar based) are needed over areas
91 where optical images are limited by persistent cloud cover (e.g., tropical areas).

92 During the last decade, synthetic aperture radar (SAR) data have been increasingly used for BA mapping as data
93 from multiple sensors became available. Such studies have taken advantage of radar independence of cloud cover and
94 solar illumination, their increased spatial resolution and the availability of multiple polarizations and incidence angles
95 (Bourgeau-Chavez et al., 2002; French et al., 1999). The European Remote Sensing (ERS) SAR satellites (ERS-1
96 and ERS-2) were widely used in boreal (Bourgeau-Chavez et al., 1997; Kasischke et al., 1994), tropical (Siegert &
97 Hoffmann, 2000; Siegert & Ruecker, 2000; Ruecker & Siegert, 2000) and Mediterranean (Gimeno et al., 2004, 2002)
98 ecosystems to detect and map BA. More recently, RADARSAT (Gimeno & San-Miguel-Ayanz, 2004; French et al.,

99 1999) and ALOS - PALSAR (Advanced Land Observation Satellite Phased Array type L-band Synthetic Aperture
100 Radar) (Polychronaki et al., 2013) were employed for the same purpose. However, past SAR missions only provided
101 data with low temporal resolution which hindered the development of efficient radar-based BA detection and mapping
102 algorithms over large areas. In addition, the utility of past sensors was limited by the available polarizations (mostly
103 single co-polarized sensors), steep viewing geometries (far from ideal when monitoring changes in vegetation) and
104 data access restrictions.

105 With the launch of ESA's Sentinel-1 satellite constellation (A and B platforms, operational since October 2014
106 and December of 2015, respectively) such limitations have been largely reduced. The Sentinel-1 constellation could
107 theoretically provide images every three days by combining datasets acquired during ascending and descending trajec-
108 tories. The independence from cloud cover and solar illumination, added to improvements in sensors characteristics
109 (e.g., dual polarization, increased spatial resolution and incidence angle, precise orbital information), provides un-
110 tapped opportunities for BA detection. A few studies have already explored the potentials of Sentinel-1 SAR images
111 for BA detection, but these studies are focused on specific regions (Engelbrecht et al., 2017; Lohberger et al., 2018).
112 To date, few studies tried integrating active and passive datasets for BA detection. Such a study detected BA in-
113 dependently from Sentinel-1 and Sentinel-2 datasets on a relatively small area in the Congo basin suggesting that a
114 combined sensor approach compensate for the strengths and limitations of each individual sensor (Verhegghen et al.,
115 2016). However, SAR based BA detection has limitations as discussed in more detail in subsection 3.2. Lastly, fusion
116 approaches combining optical and radar data have been considered for BA detection. In Stroppiana et al. (2015b,a)
117 Landsat-5 TM and C-band ENVISAT ASAR data were integrated into a fuzzy algorithm aimed at burned area detec-
118 tion in a Mediterranean environment.

119 This paper presents a novel radar-based BA mapping algorithm based on temporal series of C-band backscatter
120 coefficient, that self-adapts to local scattering conditions and it is able to detect small fires (down to 1 ha) in a fairly
121 automatic way. The specific objectives of this study were to: (i) present the proposed algorithm and explain its
122 functionalities; (ii) validate the BA detections over major biomes; (iii) compare the detection accuracy with that of
123 existing products based on passive datasets; and (iv) analyse the factors influencing the algorithm accuracy.

124 2. Study area and dataset

125 The algorithm was developed using data from four sites, three located in the Amazon basin and one located in the
126 Iberian Peninsula. Subsequently, the algorithm was validated over 18 sites around the world (Fig. 1). The validation
127 areas were located within biomes where fire events occur frequently, from boreal forests to tropical and sub-tropical
128 forests, savannas and grasslands.

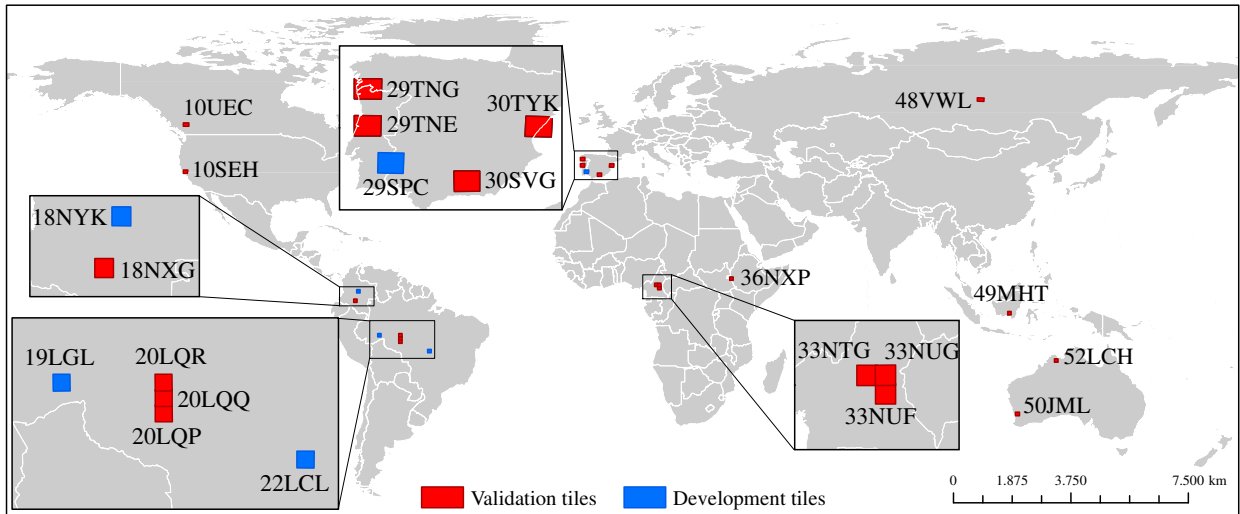


Fig. 1: Location of the Military Grid Reference System tiles used for algorithm development and validation.

The algorithm relies on temporal series of Ground Range Detected (GRD) dual-polarized (vertical-vertical VV, and vertical-horizontal VH polarizations) SAR images acquired by the Sentinel-1 A/B satellites in interferometric wide (IW) swath mode. The GRD data was processed on a tile base structure using as grid the 100×100 km Military Grid Reference System (MGRS). For each tile, Sentinel-1 images from ascending and descending passes (when available) and from all intersecting relative orbits were used. Land cover (LC) classification and hotspots derived from thermal anomalies were used as ancillary data.

The land cover classification was produced in the framework of the ESA's [Land.Cover.cci](#) project. This project delivers time series of consistent global LC maps at 300 m spacing on an annual basis from 1992 to 2015. The most recent map (i.e., 2015) was used. CCI land cover maps were generated using a combination of sensors, including MERIS and Proba-V time series of surface reflectance (Kirches et al., 2014). Since the SAR images were processed at a significantly higher pixel spacing (40 m, see subsection 3.1) than the LC map, the later was resized using a nearest-neighbour interpolation to coincide with the SAR spacing. In addition, the Land Cover Classification System (LCC) (Di Gregorio, 2005) was simplified by joining similar cover types into six groups: shrublands, grasslands, forests, crops, non-burnable, and others. One should notice that BA detection takes place over 100×100 km tiles. Therefore, for any given tile, the simplified LCC classification groups very similar classes.

Hotspots were available from NASA's Fire Information for Resource Management System (FIRMS). The hotspots were recorded by two sensors, the VIIRS (Visible Infrared Imaging Radiometer Suite) sensor at 375 m spatial resolution (Schroeder et al., 2014) and the MODIS sensor at 1 km spatial resolution (Giglio et al., 2003). The VIIRS and MODIS database was last accessed in January 2018.

To derive the validation fire perimeters (see subsection 3.4 for more details), Landsat-8 optical images were retrieved from the United States Geological Survey repository (USGS) as atmospherically corrected surface reflectance products (Vermote et al., 2016). The validation period was adjusted for each tile considering the fire season length

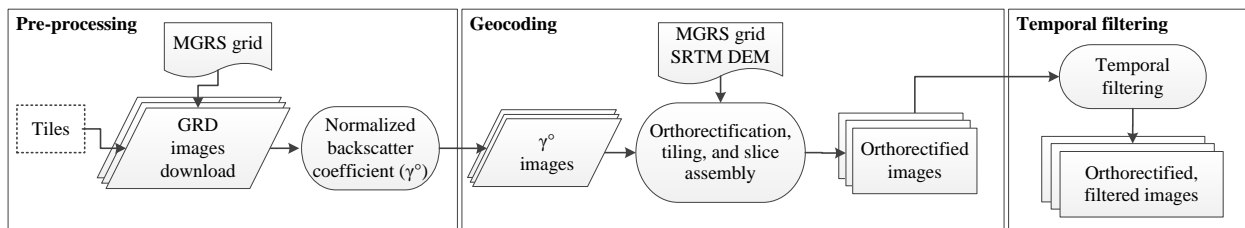
154 and the availability of Landsat images with a cloud cover under 30%. Sentinel-2 Level-1C images retrieved from
 155 the [Copernicus Open Access Hub](#) were considered to reduce temporal gaps in the validation dataset and thus large
 156 discrepancies between the validation period and the Sentinel-1 detection period.

157 The effect of soil moisture, an important factor affecting radar backscatter, on BA detection accuracy was analysed
 158 using the global Soil Moisture Active Passive (SMAP) product. Specifically, the Enhanced Level 3 Passive Soil
 159 Moisture Product based on L-Band Radiometer (9 km pixel spacing and 3 days revisit period) was used. The reliability
 160 of this product was demonstrated by a correlation coefficient above 0.8 between the estimated soil moisture and *in*
 161 *situ* measurements (Chan et al., 2018; Chen et al., 2018). From this product, the descending pass images (6 AM
 162 Equator crossing), more accurate than ascending according to Chan et al. (2018), were used so that all measurements
 163 represented the same acquisition time (Chan, 2016). As for the LC map, the product was resized to 40 m using the
 164 nearest-neighbour interpolation.

165 3. Methods

166 3.1. SAR data pre-processing

167 The Sentinel-1 data was processed using open-source libraries available in the Orfeo ToolBox (OTB), an image
 168 processing software developed by the National Centre for Space Studies (CNES), France (Inglada & Christophe,
 169 2009). The OTB-based processing chain uses Ground Range Detected (GRD) Sentinel-1 images with the SAR data
 170 being tiled to 100 km using the MGRS system. The chain is highly scalable and autonomous once few parameters are
 171 set and includes the data download from Sentinel-1 repositories. The SAR data processing may be grouped in several
 172 steps including, pre-processing, geocoding and temporal filtering (Fig. 2).



174 Fig. 2: SAR data processing with the Orfeo Toolbox.
 175

176 The pre-processing step includes data download of the specified MGRS tiles and radiometric normalization to
 177 gamma nought (γ^0) using the gamma nought lookup table provided in the product metadata. Only SAR images ac-
 178 quired in the interferometric wide swath mode, the Sentinel-1 default acquisition mode over land, were used. The
 179 calibrated images were orthorectified to ground geometry using elevation information from the Shuttle Radar Topog-
 180 raphy Mission (SRTM) one arc-second DEM and the bicubic interpolator. The orthorectified images were clipped
 181 to the processing tile and the data acquired from the same orbital path but provided within different slices were mo-
 182 saicked (i.e., slice assembly). It should be noted that the BA algorithm uses temporal backscatter differences of the

183 same relative orbit, hence, terrain-flattening (Small, 2011; Frey et al., 2013) was not necessary as the DEM-derived
184 normalization (illumination) area for a given pixel is constant in time thus not affecting the pre- to post-fire backscatter
185 coefficient variations (Tanase et al., 2010c, 2015, 2018). The last step was a multi-temporal filtering of the products
186 for each satellite pass (Quegan et al., 2000). The GRD data were processed to the nominal Sentinel-1 resolution (20
187 m) through the OTB based chain.

188 The BA detection algorithm deployment over large areas is conditioned by its performance (speed) and accuracy.
189 Both parameters are influenced by the pixel spacing to which products are processed as omission and commission
190 errors are highly depended on speckle while the processing speed increases with decreasing pixel size. Analysing
191 the effect of pixel spacing on image radiometric properties, processing time and BA detection accuracy was essential
192 for selecting the optimum pixel spacing for deployment. Tanase & Belenguer-Plomer (2018) carried out an analysis
193 for four pixel spacing (i.e., 20, 30, 40 and 50 m) over two test tiles. A 40 m spacing provided the optimum trade-off
194 between speckle reduction, storage and computing requirements and the accuracy of the detected BA. Therefore, the
195 temporally filtered images were aggregated to 40 m.

196 Radio Frequency Interference (RFI) may contaminate SAR data. Since RFI are largely observed over highly
197 populated urban areas (Li et al., 2004; Njoku et al., 2005; Lacava et al., 2013) and considering that burned areas are
198 usually located away from large cities, such effects were not observed and consequently were not considered.

199 3.2. Backscatter behaviour in burned areas

200 To better understand the proposed algorithm, its development, and the decision-making process that shaped it, this
201 subsection describes the behaviour of C-band backscatter coefficient after fire events.

202 Fire on vegetated areas results in variations of the backscatter coefficient, which may increase or decrease de-
203 pending on the polarization, the remaining vegetation and the environmental conditions (i.e., rainfall) during SAR
204 data acquisition. Fire consumption reduces the number of vegetation scattering elements potentially reducing the
205 backscatter coefficient (Van Zyl, 1993; Antikidis et al., 1998). However, biomass consumption may increase scat-
206 tering from the ground due to reduced signal attenuation (less vegetation) and the increased effect of soil surface
207 properties, such as moisture and roughness (Tanase et al., 2010b). Hence, microwaves backscatter behaviour in areas
208 affected by fires may be more heavily influenced by soil moisture properties when compared to unburned areas, par-
209 ticularly when rainfall occurs after the fire (Imperatore et al., 2017; Gimeno & San-Miguel-Ayanz, 2004; Ruecker &
210 Siegert, 2000). Rain and melting snow are the main causes of increased soil moisture (Huang & Siegert, 2006), influ-
211 encing the radar signal and consequently reducing C-band sensitivity to fire induced changes (Tanase et al., 2010b).
212 SAR-based BA mapping may be further hindered by spatial changes in soil moisture due to fire unrelated factors (e.g.,
213 temperature, insolation, wind, slope and orientation, soil roughness) which are difficult to embed into detection algo-
214 rithms. The local incidence angle (LIA) is yet another factor influencing C-band sensitivity to fire induced changes,
215 with smaller LIA values providing increased burned to non-burned differentiation for co-polarized waves (Gimeno &
216 San-Miguel-Ayanz, 2004; Huang & Siegert, 2006; Tanase et al., 2010b). Finally, wave polarization is also a funda-

217 mental variable, with cross-polarized waves being more sensitive to changes in vegetation (volumetric scattering) and
218 less to surface properties (e.g., soil moisture and roughness) when compared to the co-polarized waves (Freeman &
219 Durden, 1998; Yamaguchi et al., 2005; Van Zyl et al., 2011). Such contrasting effects may generate a wide range of
220 possible backscatter variations over burned areas that depend on the interplay between the SAR sensor characteristics
221 (e.g., wavelength, polarization, incidence angle) and environmental conditions at SAR acquisition (e.g., fire impact,
222 soil surface properties, meteorological conditions).

223 The impact of fire on the backscattering coefficient was actually found to cause ambiguous effects. A strong
224 backscatter decrease was found for burned tropical forests at C-band VV polarization under dry weather conditions
225 due to the decreased volume scattering and increased heat flux, which led to a dryer ground (Ruecker & Siegert,
226 2000; Lohberger et al., 2018). After rainfall, discrimination from the unburned surrounding forests was difficult as
227 the backscatter coefficient over BA increased (Siegert & Ruecker, 2000). In the temperate region and the Mediter-
228 ranean basin, lower backscatter values were found in fire-affected areas for cross-polarized C-band when compared
229 to adjacent unburned forest (Rignot et al., 1999; Imperatore et al., 2017). In boreal forests, higher backscatter values,
230 when compared to the adjacent unburned areas, were observed at C-band VV polarization when soil moisture was
231 high, whereas lower backscatter was observed for sites with better drainage (Bourgeau-Chavez et al., 2002; Huang &
232 Siegert, 2006; Kasischke et al., 1994). In Australian woodlands and open forests, the post-fire backscatter increased
233 for co-polarized waves and decreased for cross-polarized waves (Menges et al., 2004) while for African open forests
234 the backscatter decreased for both co- and cross-polarized C-band channels, although only the co-polarized channel
235 was deemed useful for BA detection (Verhegghen et al., 2016). Changes in the post-fire backscatter levels appear to
236 be strongly related to changes in soil moisture, with data acquired after rainfall being less suitable for classification
237 or biophysical parameters retrieval. However, some fire-related studies reported increased differentiation potential for
238 BA after rainfall in the Mediterranean basin (Gimeno & San-Miguel-Ayanz, 2004).

239 3.3. Burned area detection and mapping algorithm

240 The main requirements of the BA detection algorithm were: (i) the use of cloud insensitive satellite data (i.e.,
241 SAR); (ii) sensitivity to local burn conditions; and (iii) a high degree of automation. The algorithm was designed to
242 make use of existing datasets for training purposes by using sets of susceptible burned and unburned pixels for locally
243 dominant land cover types. The algorithm has six stages with its simplified structure being provided in Fig. 3. The
244 following paragraphs explain in detail each stage.

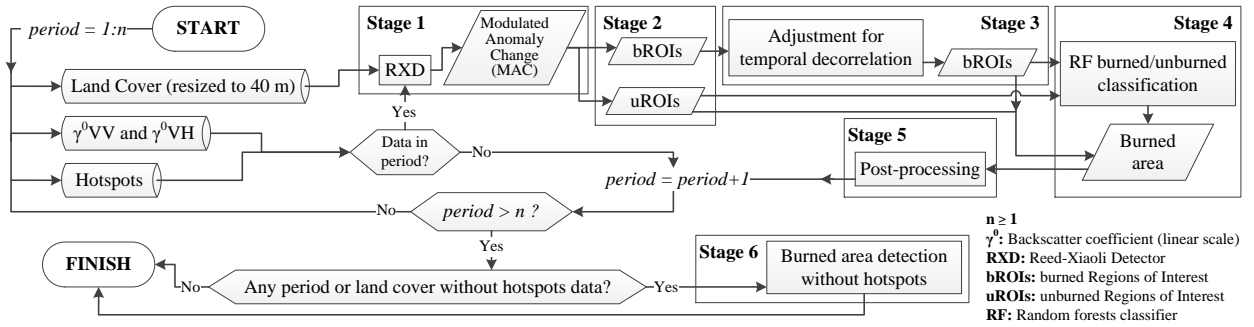


Fig. 3: Flowchart of the SAR based algorithm for burned area detection.

3.3.1. Stage 1: Anomaly change detection

An anomalous change implies variations outside the typical behaviour expected for a given area and time. Burned areas were considered anomalies since fires are inconsistent spatial and temporal events. The Reed-Xiaoli detector (RXD), proposed by Reed & Yu (1990), extracts signatures that are distinct from the surroundings without the need for *a priori* information. Anomalies have two characteristics that make them outliers: (i) spectral signatures different from the surrounding pixels; and (ii) low occurrence probability (Stein et al., 2002; Banerjee et al., 2006; Kwon & Nasrabadi, 2005). ~~RXD uses the~~ Hence, RXD allows to distinguish anomalous changes, such as burned areas, from pervasive changes, those occur in a periodical way and most part of the image, such as seasonal effects (Theiler & Perkins, 2006). The covariance matrix to calculate the Mahalanobis distance from a given pixel to the mean of the ~~no change areas surrounding~~ pixels (background) is needed by the RXD (Dabbiru et al., 2012). Thus, for any given pixel of the image, the RXD (Eq. 1) scores the Anomalous Change (AC).

$$AC(x) = (\mathbf{x} - \boldsymbol{\mu})^T \mathbf{C}^{-1} (\mathbf{x} - \boldsymbol{\mu}) \quad (1)$$

where x is any given pixel, \mathbf{x} is a vector formed by the image bands values of the pixel x , $\boldsymbol{\mu}$ is a vector composed by the mean value of the background pixels (e.g., stable areas) in each image band and \mathbf{C} is the covariance matrix of the image bands (computed from the background pixels). The background value may be computed as the mean sample of a subset image ~~where only pixels of same land cover class of x were included in order to differentiate in a easiest way the anomalous changes from the pervasive, since seasonal effects or soil moisture variations may modify backscatter coefficient differently in function of land cover class.~~ When *a priori* information is available, the background value may be computed from areas where anomalies are not expected. For BA detection, *a priori* information was provided by MODIS and VIIRS active fire databases. MODIS and VIIRS hotspots corresponding to the current detection period (CDP) were used to mask areas likely affected by fires while the remaining pixels were used to calculate the background values. The BA masks were derived by taking a buffer of 0.75 km around each hotspot. This buffer was considered the influence area of each individual hotspot (IAhs) and it roughly corresponds to the pixel size for VIIRS and MODIS thermal channels while also considering location uncertainty.

272 The RXD was applied to a set of temporal ratios of the backscatter coefficient (Eq. 2 and 3). Such temporal
 273 indices were previously used for estimating the impact of different disturbance agents (e.g., fire, insects, wind) on
 274 vegetation (Tanase et al., 2015, 2018). The selected temporal radar indices mainly use the VH backscatter, which
 275 is more responsive to volumetric scattering from vegetation and less affected by changes in surface properties (e.g.,
 276 soil moisture, surface roughness) when compared to the co-polarized (VV polarization) channel (Freeman & Durden,
 277 1998; Yamaguchi et al., 2005; Van Zyl et al., 2011).

$$278 \quad RI_1 = \gamma^0 VH_{t-1} / \gamma^0 VH_{t+1} \quad (2)$$

$$279 \quad RI_2 = (\gamma^0 VH_{t-1} / \gamma^0 VV_{t-1}) / (\gamma^0 VH_{t+1} / \gamma^0 VV_{t+1}) \quad (3)$$

280 where γ^0 is the backscatter coefficient (linear scale) of VV or VH polarizations, and $t - 1$ and $t + 1$ are respectively
 281 pre- and post-fire detection dates that define the CDP.

282 To reduce errors related to signal variation due to fire unrelated sources (e.g., variation in soils moisture, vegetation
 283 regrowth), the AC values for CDP were modulated by the AC values recorded for the previous detection period (PDP)
 284 (Eq. 4). Practically, AC scores of the PDP were subtracted from the AC of the CDP. The result was a Modulated
 285 Anomalous Changes (MAC) score used in all subsequent algorithm stages.

$$286 \quad MAC(x) = AC(x)_{[t-1..t+1]} - AC(x)_{[t-2..t-1]} \quad (4)$$

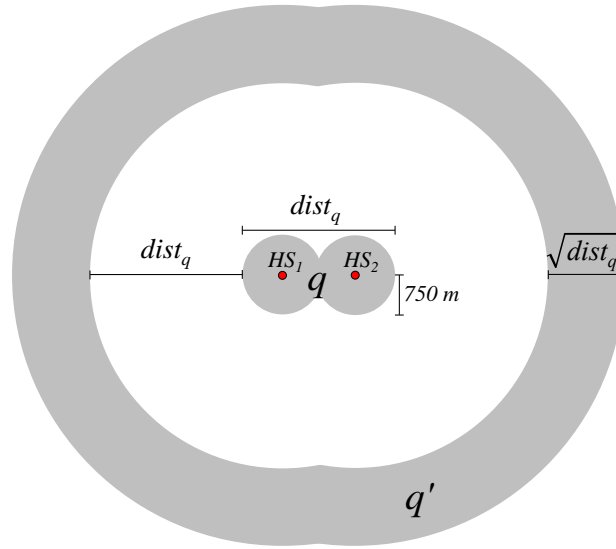
287 3.3.2. Stage 2: Burned and unburned regions of interest

288 In this stage, burned and unburned Regions of Interest (ROIs) were automatically extracted using the MAC scores
 289 and ancillary information from hotspots and land cover data. Since information on hotspots was acquired daily from
 290 two independent sensors (VIIRS and MODIS) most burned pixels in the selected study areas (94.3%) were in fire
 291 patches with at least one hotspot within 0.75 km, the selected buffer considered as hotspot area of influence (IAhs)
 292 even for the tropical regions, where cloud cover is frequent. The presence of hotspots greatly facilitated the attribution
 293 of the detected MAC values to burned areas. This allowed distinguishing BA from other changes, such as logging, crop
 294 harvesting, flooding, or vegetation disturbance due to insects or diseases. When hotspots were not available, due to the
 295 cloud cover or small fire size, a different attribution method was used as explained in Stage 4. Burned ROIs (bROIs)
 296 were extracted in two steps: seeding and growing. This is an approach previously used for BA mapping algorithms
 297 (Bastarrika et al., 2011; Alonso-Canas & Chuvieco, 2015; Roteta et al., 2019). To obtain the seeds, spatially connected
 298 IAhs pixels were first grouped in uniquely identified objects: $q_1 : n$, where n is the number of the unique objects. A
 299 pixel x inside an object q , was considered burned seed (bSeed) if Eq. 5 was met.

$$300 \quad x = \text{bSeed}(q) \rightarrow (\text{MAC}(x) \geq \min(s, v) > 0) \vee (\text{MAC}(x) \geq \max(s, v) > 0 \wedge \min(s, v) < 0) \quad (5)$$

301 where $s = \mu(\text{MAC}_{q'})$, being μ the mean and q' a region around q bounded by $dist_q$ and $dist_q + \sqrt{dist_q}$, with $dist_q$ being
 302 the maximum span of object q . Thus, q' delineates likely unburned areas in the vicinity of q ; and $v = \mu(\text{MAC}_{N_G})$,
 303 with N_G being the neighbour pixels of G , where G is a pool of pixels inside q with MAC values below $\mu(\text{MAC}_q)$.
 304 Essentially, for a pixel to be considered seed it had to fulfil two conditions, one related to vicinity to a hotspot (within
 305 IAhs) and the second related to the magnitude of backscatter change (MAC score).

306 The bSeed pixels were extracted considering the major land cover type for each q object. Therefore, pixels in
 307 q' region were stratified by land cover type with only pixels of the same land cover type as predominant of q being
 308 used for computations. In addition, the selected q' pixels needed to be outside the IAhs of any other hotspot. Fig. 4
 309 shows graphically the concepts of q , q' and $dist_q$. Once bSeed pixels for q were extracted, an open morphological
 310 operator (3×3 window) was used to eliminate isolated bSeed pixels. With increasing window size, BA omission
 311 errors increased while commission errors decreased. To determine the optimum size, an error analysis was carried out
 312 using different window sizes (3×3 , 5×5 and 7×7) over the four algorithm development tiles (analysis not shown).
 313 The 3×3 window was selected since it least affected the detection of small size fires while still managing to reduce
 314 commission errors. The same window size was used in previous works to reduce speckle effects (Menges et al., 2004).



315

316 Fig. 4: Graphical representation of concepts needed to extract bROIs, being HS - hotspot.
 317

318 Given an object q and its predominant land cover class k , the growing phase started by masking out all the pixels
 319 of the image which MAC values were below the mean MAC value of all image pixels of land cover class k . The
 320 remaining pixels were used to compute a new mean of the MAC values which was used as the minimum threshold to
 321 label Likely Burned Pixels (LBP) of q (Eq. 6).

$$322 \quad x = \text{LBP}(q) \rightarrow \text{MAC}(x) > \mu(\text{MAC} > \mu(\text{MAC}_k)) \quad (6)$$

323 Connected LBP(q) pixels were grouped and subsequently overlapped with the extracted bSeed pixels of q . LBP(q)
324 groups overlapping bSeed pixels of q were assigned to the bROIs and constituted the first component of the de-
325 tected burned areas. The second component was detected using no parametric classification (i.e., random forests) as
326 explained in [Stage 4](#).

327 The unburned ROIs (uROIs) were derived iteratively by land cover type. The histogram of bROIs pixels identified
328 in the previous step was used to calculate the MAC values for the 25 and 75 percentiles (P_{25} and P_{75} , respectively).
329 These values constituted thresholds used to classify the MAC image in burned and unburned. Pixels with MAC values
330 below P_{25} or above P_{75} were considered possible unburned seeds since: (i) MAC values below P_{25} indicate small
331 changes, likely unrelated to fires (e.g., vegetation growth, changes in vegetation water content); and (ii) MAC values
332 above P_{75} are usually associated with significant changes, such as logging, crop harvesting, or floods. One should
333 note that, high severity fires may also result in MAC values above P_{75} . However, such areas are regularly associated
334 to hotspots and therefore were not labelled as uROIs. An open morphological operator (3×3 window) was applied to
335 the classified binary image to remove noise. The effect of the open morphological operator was an increased number
336 of unburned pixels. Pixels from the not burnable LC map classes (i.e., bare soils, water, snow and ice, urban areas)
337 were labelled as uROIs, while pixels overlapping IAhs or bROIs were filtered out. Additionally, for the crop land
338 cover class, groups of pixels over 56 ha (0.75×0.75 km, being 0.75 km the double of VIIRS spatial resolution) not
339 overlapping hotspots were included as uROIs to account for fire-unrelated changes, such as crop harvesting or changes
340 in surface properties (roughness) due to agricultural works (e.g., ploughing).

341 3.3.3. Stage 3: Adjustment for temporal decorrelation

342 During algorithm development, a temporal decorrelation between fire events (i.e., hotspots date) and backscatter
343 coefficient change was observed ([Belenguer-Plomer et al., 2018b](#)). Such decorrelation events may be the result of
344 delayed backscatter decrease after fire due to multiple factors including: (i) pre-fire conditions, e.g., drier than usual
345 weather may result in low values for the pre-fire backscatter coefficient; (ii) post-fire weather, e.g., precipitations
346 may temporally increase the backscatter coefficient; and (iii) vegetation-dependent backscatter response to fire events.
347 For example, over forests, VH backscatter decrease may be delayed as there are still sufficient scattering elements
348 (tree trunks and branches) present after fire. As time passes, trunks and branches dry up, which results in decreased
349 backscatter from vegetation.

350 To account for temporal decorrelation the BA was detected iteratively for each period. Delayed changes in
351 backscatter were accounted for computing the bROIs detected in periods formed by the current pre-fire image ($t - 1$)
352 and images acquired during following 90 days past the CDP (i.e., $t + 2$, $t + 3$). This temporal threshold was based on
353 empirical observations ([Belenguer-Plomer et al., 2018b](#)). Such bROIs were labelled as burned in the CDP ($t - 1$ to
354 $t + 1$) when overlapping hotspots from the CDP. Additionally, these bROIs must not overlap hotspot recorded past the
355 CDP.

356 3.3.4. Stage 4: Random forests burned / unburned classification

357 Only a fraction of the anomalous pixels was labelled as burned based on information from hotspots due to the
358 rather restrictive criteria (i.e., MAC score) used in Stage 2 and 3. Pixels not meeting the imposed criteria also needed
359 labelling. To avoid subjectivity, such pixels were labelled using a non-parametric classifier (i.e., random forests)
360 trained with data extracted from bROIs and uROIs by each land cover classes and CDP. The random forests (RF)
361 classifier was used as it is robust to data noise (Gislason et al., 2006; Rodriguez-Galiano et al., 2012; Du et al., 2015;
362 Waske & Braun, 2009) and less sensitive, when compared to other machine learning techniques, to the quality of
363 training samples and overfitting (Belgiu & Drăguț, 2016). Moreover, RF was already used to classify SAR data
364 (Waske & Braun, 2009) and solve similar fire mapping problems (Collins et al., 2018; Fernandez-Carrillo et al., 2018;
365 Ramo & Chuvieco, 2017; Meddens et al., 2016).

366 RF is an ensemble classifier that consists of a group of decision trees $\{h(\mathbf{x}', \Theta_z), z = 1, \dots\}$, where \mathbf{x}' is the input
367 vector of any given pixel (x), and Θ_z are an independently bootstrap sampled vectors with replacement in each decision
368 tree (z). Each tree provides a unique class for x , being the class of x assigned as the most popular voted class (Breiman,
369 2001). In this study, *TreeBagger* from MATLAB[®] software package was used to construct the RF classifiers.

370 RF classifiers are customizable through different parameters, such as: (i) number of trees; (ii) number of training
371 samples; (iii) proportion of training samples by class; and (iv) number of independent variables employed in each tree.
372 The number of trees is a key adjustment in RF classification since for more trees the generalization error converges
373 and models are not over-fit (Breiman, 2001; Pal, 2005; Rodriguez-Galiano et al., 2012). On the other hand, using more
374 trees demands more computational resources. An empirical analysis (not shown) concluded that 250 trees provided
375 the best trade-off between speed and accuracy for BA classification in this study. Since the number of pixels in
376 bROIs and uROIs is high, computational costs may be reduced by using just a fraction for training purposes. This
377 fraction was determined, by land cover classes, as 1% of all bROIs and uROIs pixels divided by the number of trees
378 (250). Unbalanced training samples may result in infra-classification of the minority classes. According to Chen et al.
379 (2004), several approaches may be used to address such problems: (i) reducing the overall learning cost, with high
380 costs being assigned to the miss-classification of the minority classes (Pazzani et al., 1994); (ii) under-sampling the
381 majority and over-sampling the minority classes; or (iii) a combination of both techniques (Chawla et al., 2002). The
382 latter approach was used in this study. Depending on the misclassification cost, the *TreeBagger* function generated
383 in-bag samples by oversampling the burned class and under sampling the unburned class. The proportion of training
384 data was empirically adjusted to 40% and 60% for burned and unburned classes, respectively.

385 The number of variables considered for trees growing in each split was computed as the square root of the total
386 number of variables (Gislason et al., 2006), as it reduces the correlation of trees and thus improves global accuracy
387 (Rodriguez-Galiano et al., 2012; Gislason et al., 2006). In addition to the SAR based metrics used for RXD (Eq. 2
388 and 3), up to 30 SAR metrics were used for RF classification. These metrics were computed as in Eq. 7 to 12. The
389 non-parametric classification was carried out considering the land cover type with specific models being built for each

390 land cover class. The BA detected by RF was added to bROIs detected in [Stage 2](#) and [3](#), and formed the total BA for
 391 the CDP.

$$392 \mu(\gamma^0 XY_{[t',t-1]}) - \gamma^0 XY_{t+i} \quad (7)$$

$$393 \mu(\gamma^0 XY_{[t',t-1]}) / \gamma^0 XY_{t+i} \quad (8)$$

$$394 \gamma^0 XY_{t-1} - \gamma^0 XY_{t+i} \quad (9)$$

$$395 \gamma^0 XY_{t-1} / \gamma^0 XY_{t+i} \quad (10)$$

$$396 (\gamma^0 VH_{t-1} / \gamma^0 VV_{t-1}) / (\gamma^0 VH_{t+i} / \gamma^0 VV_{t+i}) \quad (11)$$

$$397 \mu(\gamma^0 VH_{[t',t-1]} / \gamma^0 VV_{[t',t-1]}) / (\gamma^0 VH_{t+i} / \gamma^0 VV_{t+i}) \quad (12)$$

398 where $\gamma^0 XY$ is the backscatter intensity (linear scale) of VV and VH polarizations, t' is $t - 1$ minus the double of days
 399 distance between $t - 1$ and $t + 1$, and i is 1 or 2, being 30 the maximum number of indices computed.

400 3.3.5. Stage 5: Post-processing

401 Post-processing was needed to account for temporal decorrelation and improve detection results over problematic
 402 land covers such as cropping areas. To adjust for temporal decorrelation, the BA detected by the non-parametric
 403 classifier for the CDP was compared to the IAhs of previous detection periods, up to 90 days before the pre-fire
 404 image ($t - 1$) ([Belenguer-Plomer et al., 2018b](#)). If burned areas detected in the current CDP (i.e., objects formed by
 405 contiguous pixels) overlapped previous IAhs (objects) by more than 75% (set from empirical observations) they were
 406 masked out and considered previous burns. Three additional post-processing steps were then carried out to further
 407 improve the results: (i) on cropping lands, groups of burned pixels (objects) with areas above 56 ha (see [Stage 2](#))
 408 that did not overlap IAhs (i.e., no local hotspot) were removed. The rationale was that lack of hotspots over a large
 409 changing cropping area is an indication of harvesting rather than fire; (ii) burned objects below one hectare were
 410 removed to reduce noise in BA detections due to residual speckle; and (iii) a modal filter with a convolution kernel of
 411 3×3 pixels was applied to smooth the salt and pepper effects typical for SAR based classifications.

412 Post-processing also deals with joining the BA detected in the different relative orbits intersecting a specific tile.
 413 The BA was detected separately for each relative orbit, to avoid misinterpreting backscatter changes due to chang-
 414 ing azimuth angles or illumination geometry as fire related changes, ~~and the results were subsequently~~. To cope the
 415 topographic effects for BA detection ([Gimeno & San-Miguel-Ayanz, 2004](#); [Huang & Siegert, 2006](#); [Tanase et al., 2010b](#))
 416 , the results from different relative orbits were combined by joining the BA detected ~~in all relative orbits~~.

417 3.3.6. Stage 6: Burned area detection without hotspots

418 As clouds may prevent the propagation of radiation from active fires to the thermal sensors on board satellites, the
 419 algorithm was built with a backup mechanism to cope with the absence of hotspots for a specific land cover type and
 420 detection period. However, for the algorithm to work, hotspots need to be available for each land cover class at some

421 point during the analysed fire season.

422 The algorithm first detected the BA for all land cover types during detection periods for which hotspots were avail-
423 able. For detection periods without hotspots, the data were temporally stored for later processing. During detection,
424 the algorithm saved a database containing the P_{25} and P_{75} of MAC values for bROIs (Stage 2) and the trained RF
425 models (Stage 4) for each land cover class. This database is hereafter referred to as the Classifier Model and Criteria
426 (CMC). Once detections for land cover classes and detection periods with hotspots ended, the CMC database was
427 used to classify the temporally stored data (i.e., land cover types without hotspots during detection periods) if two
428 conditions were met: (i) the CDP was within the fire season. The length of the fire season was computed using the
429 hotspots daily frequency as the interval between the dates corresponding to the P_5 and P_{95} ; and (ii) the difference
430 between the CDP and the date for the nearest CMC was less than one month, thus avoiding possible confusions due
431 to changes in vegetation phenology. When CMC entries from different detection periods met the conditions, the one
432 closest to the CDP was used. The MAC image for the CDP was segmented into possibly burned and unburned based
433 on the CMC P_{25} and P_{75} , with the possible burned pixels being subsequently classified using the stored RF models by
434 land cover class. When CMC entries were spaced equally in time when compared to the CDP (i.e., one entry is from
435 a previous period and one from a posterior period), each entry was used separately and only the commonly detected
436 BA was kept. The post-processing operations from Stage 5 were carried out on the detected BA from this stage.

437 An additional operation was carried out to reduce possible commission errors during this stage. The operation was
438 carried out over BA detected on different relative orbits. Note that detections were always carried out using time-series
439 of images from the same relative orbit. If several relative orbits intersected a given tile, the algorithm worked through
440 the data from each relative orbit separately. BA products composites were subsequently formed using detections from
441 different relative orbits and the same detection period. For each detection period, BA pixels detected in different
442 relative orbits were grouped in objects. If all pixels of an object were classified as unburned in one orbit, the object
443 was removed from the detected BA for the CDP. Since, dual pass (ascending and descending) acquisition were not
444 available for all tiles and spatially overlapping relative orbits only partially covered any given tile, this additional
445 operation reduced commission errors where BA detections intersected.

446 3.4. Reference images and validation metrics

447 The reference burned perimeters extraction for validation purposes was based on a well established framework
448 (Padilla et al., 2014, 2015, 2017). The reference data were obtained from Landsat-8 images using a RF classifier and
449 training polygons selected by an independent operator. The validation perimeters were generated from 120 multi-
450 temporal pairs of images with a maximum separation of 32 days. The temporal separation of the pairs was short
451 to ensure that fire scars were clearly visible in the post-fire image. Before running the classification, clouds were
452 removed using the pixel quality band of the Landsat product and each pair of images was clipped to the extent of its
453 corresponding MGRS tile. Training areas were selected using a false colour composite (RGB: SWIR, NIR, R) that
454 allowed for a clear discrimination of burned areas. Three training classes were considered: burned, unburned and no

455 data.

456 The variables selected as input for the RF classifier were: (i) Landsat-8 bands 4 and 7; (ii) the Normalized Burn
 457 Ratio (NBR); and (iii) the temporal difference between the pre- and post-fire NBR values (dNBR). The NBR (Eq. 13)
 458 is defined as the normalized difference between the reflectance of NIR and SWIR wavelengths (García & Caselles,
 459 1991; Key & Benson, 2006).

$$460 \text{NBR} = (\text{Band 4} - \text{Band 7}) / (\text{Band 4} + \text{Band 7}) \quad (13)$$

461 where Band 4 is the surface reflectance in the near infra-red (NIR) wavelength (0.772 - 0.898 μm) and Band 7 is the
 462 surface reflectance in the shortwave infra-red (SWIR) wavelength (2.064 - 2.345 μm).

463 After the RF classification, fire perimeters were visually revised to correct possible errors. New training fields
 464 were iteratively added and the RF was re-run until the classification result were deemed accurate. Reference BA
 465 perimeters were resized using a nearest-neighbour interpolation to the selected pixel spacing of the Sentinel-1 product
 466 (40 m). Temporal gaps between the Landsat-8 reference period and the Sentinel-1 detection period were filled in
 467 through photo-interpretation of Sentinel-2 images.

468 The Sentinel-1 BA detections were validated using confusion matrices (Table 1). Three accuracy metrics were
 469 computed for the burned area class using the confusion matrices, the omission error (Eq. 14), the commission error
 470 (Eq. 15) and the Dice coefficient (Eq. 16) (Padilla et al., 2015).

471 Table 1: Confusion matrix example.

Detection	Reference data		Row total
	Burned	Unburned	
Burned	P_{11}	P_{12}	P_{1+}
Unburned	P_{21}	P_{22}	P_{2+}
Col. total	P_{+1}	P_{+2}	N

$$474 \text{OE} = P_{21}/P_{+1} \quad (14)$$

$$475 \text{CE} = P_{12}/P_{1+} \quad (15)$$

$$476 \text{DC} = 2P_{11}/(P_{1+} + P_{+1}) \quad (16)$$

477 **4. Results**

478 *4.1. Algorithm accuracy*

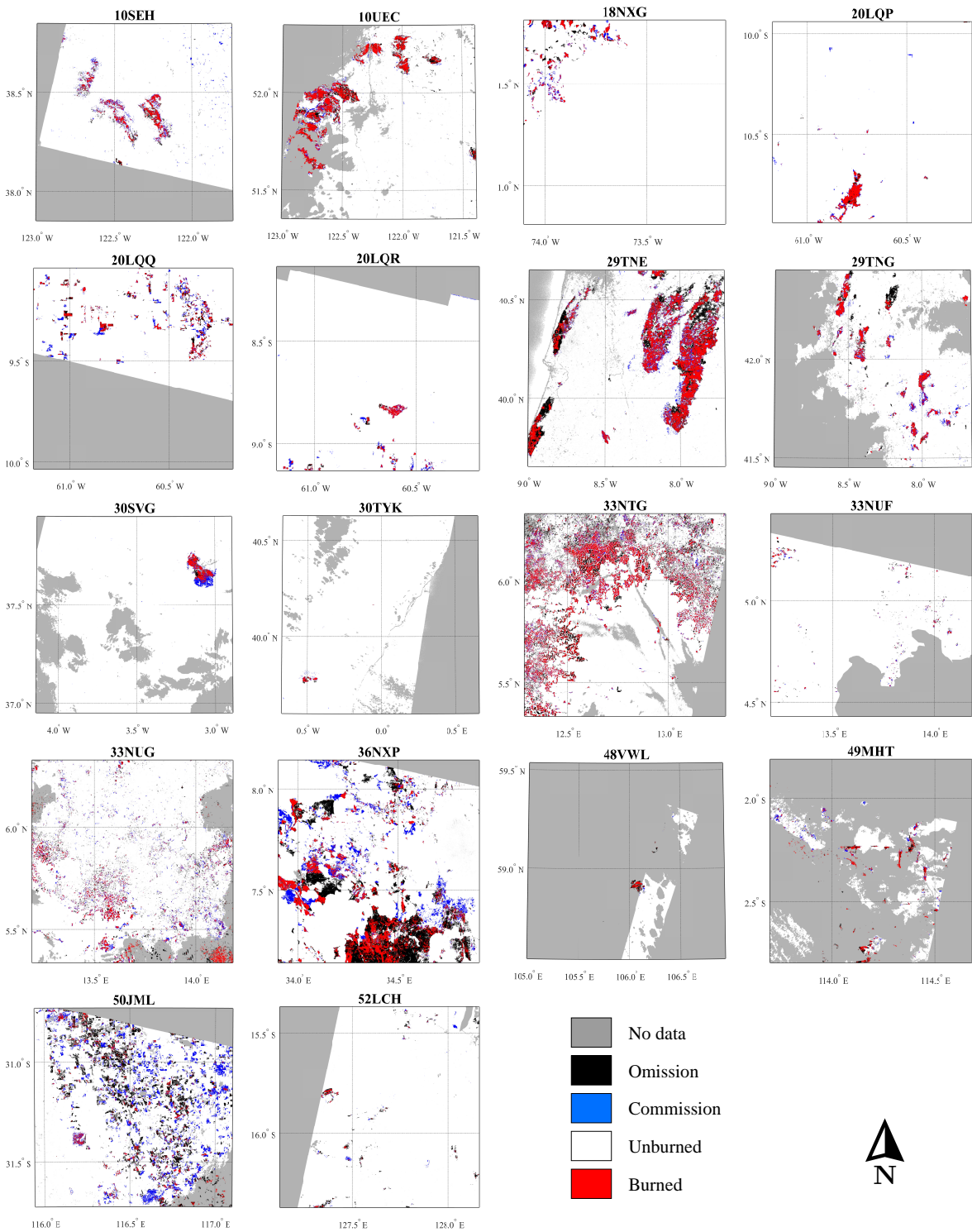
479 The OE and CE over the validation tiles varied, with the highest errors (0.54 to 0.81) being observed over Aus-
480 tralian grasslands and the lowest (0.19 to 0.2) over the Mediterranean forests and shrublands (Table 2). The highest
481 BA detection accuracy (DC 0.82) was observed over the tile 22LQP located in the Amazon basin (Fig. 5). By land
482 cover type, the algorithm produces more accurate results over forested areas (DC 0.64), followed by shrublands (DC
483 0.56). The lowest detection accuracy was observed over grasslands (DC 0.28) (Fig. 6). Note that error metrics by land
484 cover type were computed by pooling pixels with the same land cover type from all tiles.

485
486

Table 2: Error metrics for Sentinel-1 burned area detections for each MGRS tile analysed.

MGRS	Reference period	Detection period	P	Dd	nIM	LC	C	DC	OE	CE
10SEH	04/10/2017–05/11/2017	28/09/2017–03/11/2017	B	12	16	G	NA	0.61	0.34	0.43
10UEC	05/07/2017–22/08/2017	08/07/2017–25/08/2017	B	12	32	F	NA	0.76	0.31	0.16
18NXG	30/10/2016–02/03/2017	03/11/2016–03/03/2017	A	24	6	F	SA	0.64	0.35	0.36
20LQP	20/07/2016–22/09/2016	03/07/2016–25/09/2016	D	84	4	F	SA	0.82	0.14	0.22
20LQQ	04/07/2016–22/09/2016	03/07/2016–25/09/2016	D	36	5	F	SA	0.55	0.42	0.48
20LQR	04/07/2016–25/09/2016	03/07/2016–25/09/2016	D	36	8	F	SA	0.64	0.26	0.43
29TNE	05/10/2017–06/11/2017	04/10/2017–04/11/2017	B	6	24	S	Eu	0.7	0.38	0.2
29TNG	05/10/2017–06/11/2017	04/10/2017–05/11/2017	B	6	24	S	Eu	0.67	0.36	0.3
30SVG	30/06/2015–16/07/2015	26/06/2015–20/07/2015	B	12	9	S	Eu	0.65	0.19	0.46
30TYK	12/06/2017–30/07/2017	10/06/2017–28/07/2017	B	12	26	S	Eu	0.69	0.31	0.3
33NTG	28/11/2015–16/02/2016	21/11/2015–13/02/2016	A	12	14	F	Af	0.63	0.47	0.21
33NUF	07/12/2015–23/12/2015	28/11/2015–22/12/2015	A	12	3	F	Af	0.52	0.52	0.43
33NUG	21/11/2015–24/01/2016	16/11/2015–27/01/2016	A	12	8	F	Af	0.52	0.52	0.44
36NXP	30/12/2016–15/01/2017	01/01/2017–26/01/2017	D	6	6	S	Af	0.46	0.62	0.41
48VWL	12/06/2017–21/06/2017	11/06/2017–23/06/2017	D	12	3	F	As	0.58	0.57	0.15
49MHT	02/07/2015–04/09/2015	26/06/2015–06/09/2015	D	24	5	O	As	0.67	0.35	0.32
50JML	07/03/2017–10/05/2017	04/03/2017–15/05/2017	D	12	13	G	Au	0.21	0.81	0.76
52LCH	05/04/2017–21/04/2017	26/03/2017–24/04/2017	D	12	7	S	Au	0.31	0.78	0.51

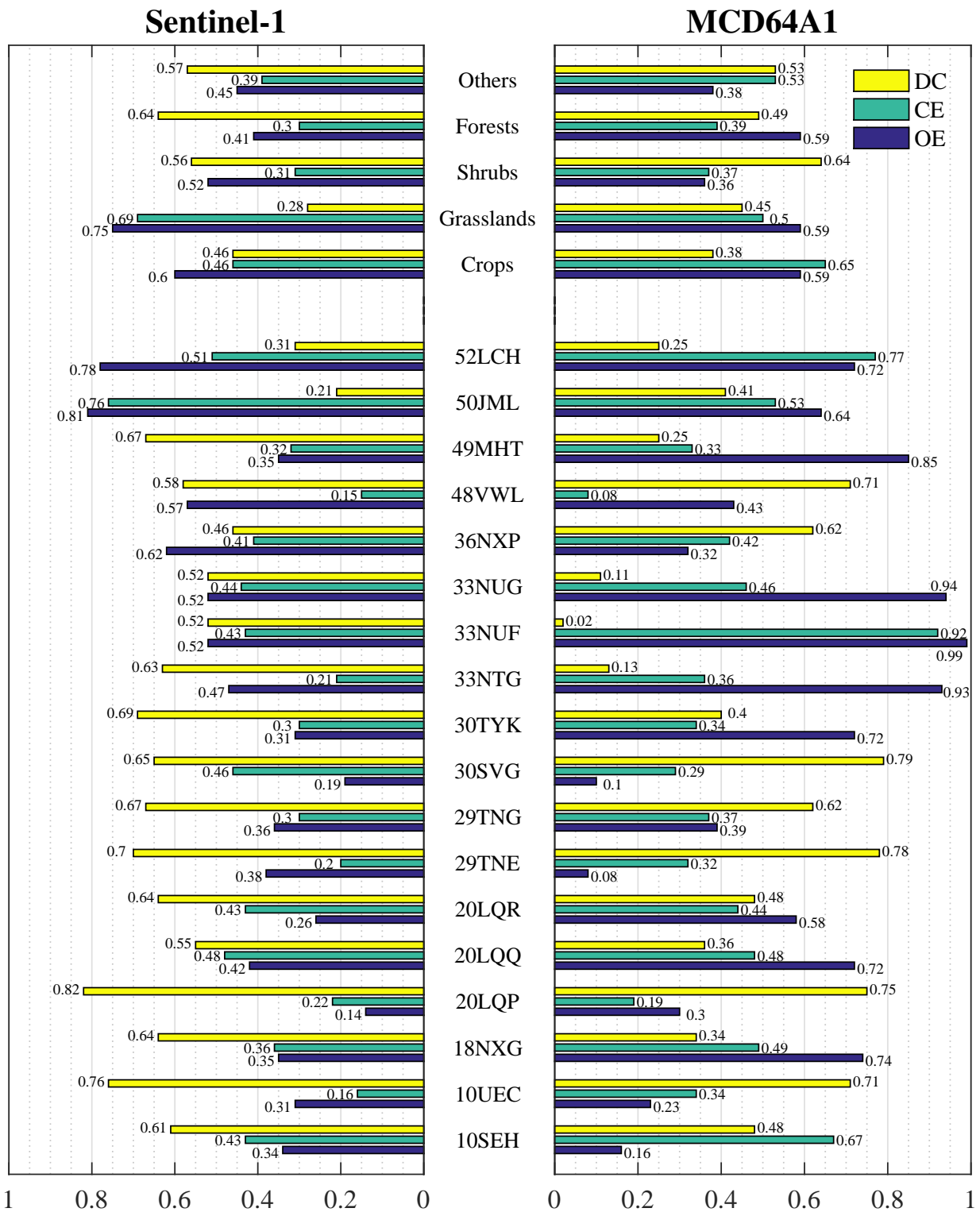
488 Reference period - period for which the reference burn perimeter were derived; Detection period - first and last
489 Sentinel-1 images of the data series; P - satellite pass (A-ascending, D-descending, and B-both); Dd - day difference
490 between images (mode); nIM - number of SAR images within the detection period; LC - predominant land cover
491 (G-grassland, S-shrub, F-forest, and O-others); C - continent for each tile (NA-North America, SA-South America,
492 Eu-Europe, Af-Africa, As-Asia, and Au-Australia); DC - Dice coefficient; OE - omission error; and CE - commission
493 error.



494

495 Fig. 5: Maps of burned area detected using Sentinel-1 data per MGRS tiles. Errors of omission and commission are also shown.

496



497

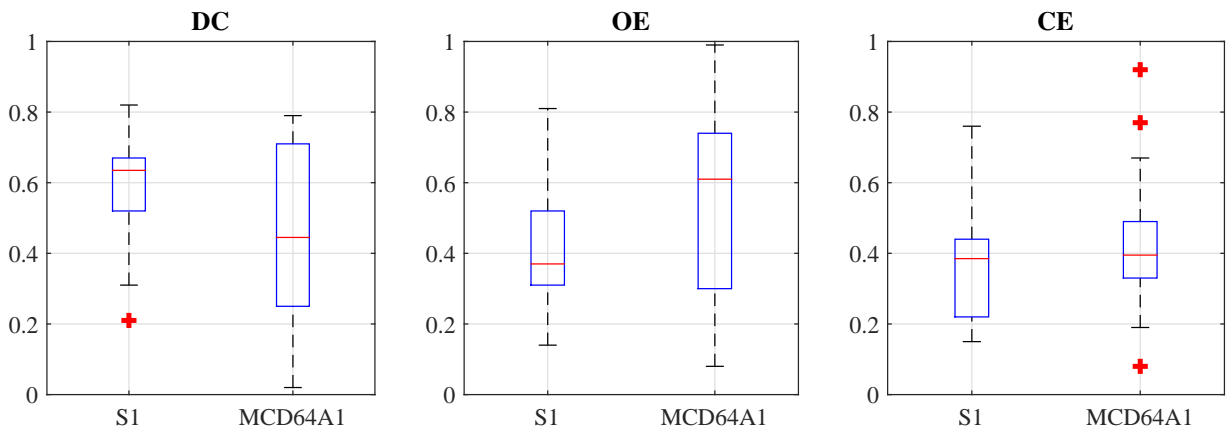
498 Fig. 6: Assessment metrics of Sentinel-1 and MCD64A1 Version 6 burned area detections per MGRS tiles and land cover classes. The metrics
 499 by land cover were computed using confusion matrices formed by pixels of the same land cover class from all tiles. DC - Dice coefficient, OE -
 500 omission error and CE - commission error.

502

503 *4.2. Comparison with existing global products*

504 The accuracy metrics of the Sentinel-1 BA detections obtained from the presented algorithm were compared to
505 those derived from the current most widely used BA global product, the MCD64A1 Version 6 (Giglio et al., 2018).
506 The magnitude of the error metrics may be influenced by the temporal match between the images used to generate the
507 reference perimeters and those used to generate the BA products. To account for detection errors caused by slightly
508 different validation and detection periods, the MCD64A1 product was temporally subset to match the Sentinel-1
509 detection periods.

510 The accuracy metrics were analysed by tile as well as by land cover classes. The tile-based analysis showed
511 particularly poor results for the MCD64A1 product over the tiles 18NXG, 20LQQ, 20LQR, 30TYK, 33NTG, 33NUF
512 and 33NUG (Fig. 6). For the remaining tiles, the accuracy of the two BA detection algorithms were closely matched,
513 with some tiles being more accurately estimated by the Sentinel-1 algorithm while others by the MCD64A1. By
514 land cover class, the MCD64A1 achieved higher accuracies over grasslands while the Sentinel-1 detections were
515 considerably more accurate over forests. For the remaining land cover classes both products showed similar accuracies
516 over burned areas. Overall, the BA was more accurately detected using the SAR based algorithm. On average Sentinel-
517 1 detections improved the DC of the MCD64A1 product from 0.46 ± 0.11 to 0.59 ± 0.06 (\pm confidence interval, 95%)
518 and reduced the OE from 0.55 ± 0.14 to 0.43 ± 0.08 and CE from 0.43 ± 0.08 to 0.37 ± 0.06 (Fig. 7).



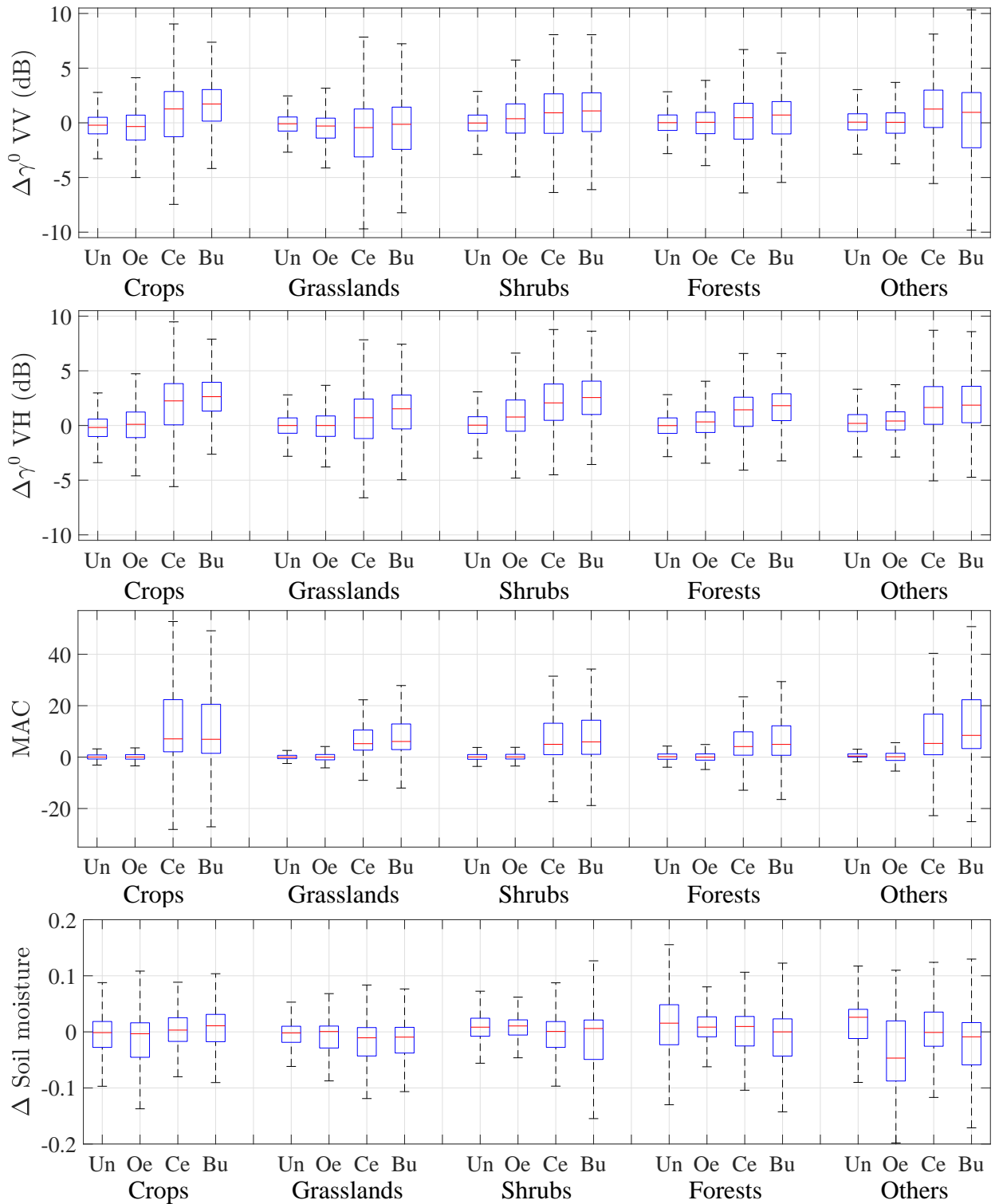
519
520 Fig. 7: Dispersion of Dice coefficient (DC), omission and commission errors (OE and CE) of burned area detected for all tiles for Sentinel-1 (S1)
521 and MCD64A1 Version 6. The red line indicates median value, and top and bottom box edges indicate the 75th and 25th percentiles, respectively,
522 while red dots indicate outliers.

523

525 *4.3. Factors influencing the algorithm accuracy*

526 The MAC values (Eq. 4), and the temporal variation (pre- minus post-fire date) of backscatter coefficient and
527 soil moisture were analysed by land cover class for each Sentinel-1 temporal pair after the BA classification. Four
528 categories were studied: burned, unburned, commission and omission errors. Data from all tiles were pooled (Fig. 8).
529 The analysis confirmed that, over burned and commission error pixels, VH backscatter mean variation was higher

530 (1.72 ± 0.002 dB) when compared to the VV polarization (0.34 ± 0.0023 dB) for all land cover classes. As expected,
531 MAC values were on average considerably higher over burned pixels and commission errors (13.5 ± 0.15) when
532 compared to unburned and omission errors pixels (0.17 ± 0.03), following the trends observed for VH backscatter
533 coefficient mean variation. Soil moisture variations from the SMAP product were very similar between burned and
534 unburned pixels with no particular trend being apparent. For crops and shrubs soil moisture variations was slightly
535 higher over burned areas while for the other land cover classes the opposite was true (Fig. 8).



536

537 Fig. 8: Temporal variation ($\Delta = data_{pre} - data_{post}$) of the backscatter coefficient (dB) and soil moisture (from SMAP) between pre- and post-dates
 538 for BA detection periods. MAC values from RXD are also presented. Values are displayed by land cover classes for four categories of pixels:
 539 unburned (Un), burned (Bu) and commission (Ce) and omission errors (Oe). Red line indicates median value. Top and bottom box edges indicate
 540 the 75th and respectively the 25th percentiles. Outliers not shown to improved graphs discernibility.
 542

543 Since the algorithm uses hotspots derived from thermal sensors to map BA, the accuracies metrics (by land cover
544 class) of the pixels located within and outside the IAhs were also compared (Table 3). The highest BA accuracy
545 (DC) and lowest omission and commission errors were observed for the pixels located within the IAhs over all land
546 cover classes as expected. Likewise, VH and VV pre- to post-fire backscatter coefficient temporal differences were
547 also compared for both cases. Similar trends, as observed in Fig. 8, where burned and commission error pixels had a
548 significant higher variation when compared to unburned and omission errors pixels, were found over both polarizations
549 independently of the location with respect to the IAhs.

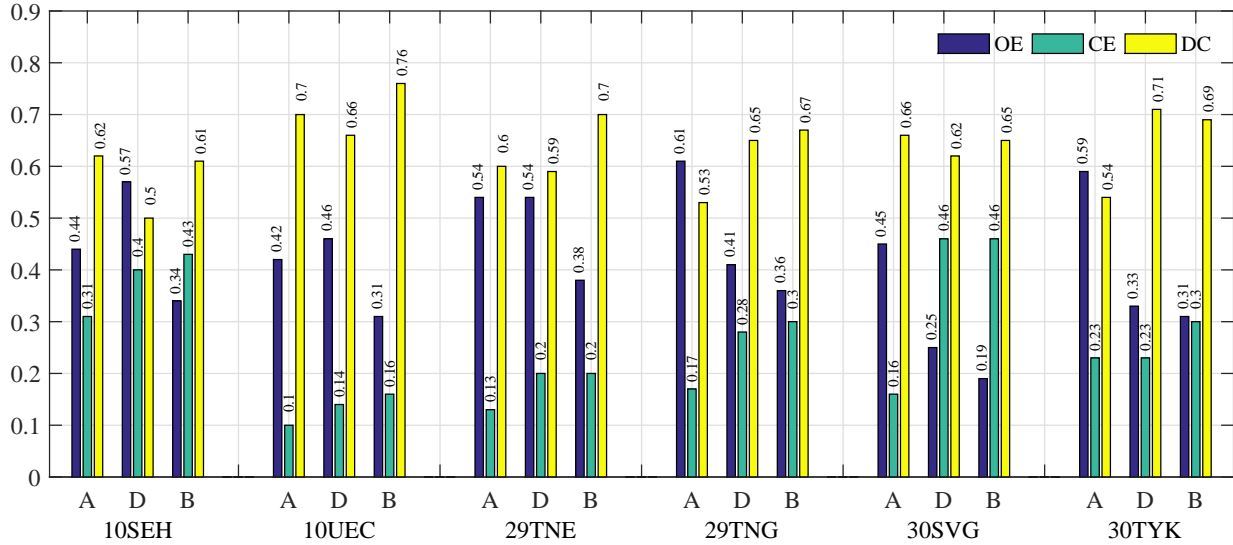
550 Table 3: Errors metrics for Sentinel-1 BA detections and pre- to post-fire backscatter variations assessed as a function of proximity with respect to
551 the hotspots influence area (IAhs).
552

		Crops	Grasslands	Shrubs	Forests	Others
	DC	0.55	0.34	0.63	0.71	0.61
	CE	0.38	0.64	0.27	0.27	0.36
	OE	0.5	0.68	0.45	0.32	0.43
Inside IAhs	Δ VH (bp)	2.52 ± 0.02	1.06 ± 0.01	2.24 ± 0.005	1.48 ± 0.003	2.33 ± 0.03
	Δ VH (cp)	1.27 ± 0.03	0.64 ± 0.01	1.54 ± 0.01	0.91 ± 0.01	1.26 ± 0.03
	Δ VH (op)	0.15 ± 0.01	-0.33 ± 0.01	0.98 ± 0.003	0.31 ± 0.002	0.43 ± 0.01
	Δ VV (bp)	1.42 ± 0.02	-0.73 ± 0.02	0.66 ± 0.01	0.26 ± 0.003	0.84 ± 0.04
	Δ VV (cp)	0.03 ± 0.03	-0.91 ± 0.01	0.21 ± 0.01	-0.13 ± 0.01	0.42 ± 0.04
	Δ VV (op)	-0.29 ± 0.01	-0.78 ± 0.01	0.61 ± 0.004	0.06 ± 0.002	-0.1 ± 0.01
	Outside IAhs	DC	0.11	0.17	0.39	0.27
CE		0.84	0.79	0.44	0.56	0.54
OE		0.92	0.86	0.7	0.81	0.57
Δ VH (bp)		2.6 ± 0.09	1.2 ± 0.03	3.63 ± 0.01	2.25 ± 0.01	0.9 ± 0.05
Δ VH (cp)		3.31 ± 0.04	0.33 ± 0.02	3.39 ± 0.01	2.18 ± 0.02	3.33 ± 0.08
Δ VH (op)		-0.01 ± 0.02	0.08 ± 0.01	0.81 ± 0.01	0.22 ± 0.004	0.52 ± 0.02
Δ VV (bp)		0.46 ± 0.11	-0.53 ± 0.03	1.73 ± 0.01	0.27 ± 0.02	-1.44 ± 0.07
Δ VV (cp)	2 ± 0.05	-1.34 ± 0.02	2.03 ± 0.01	1.21 ± 0.02	2.78 ± 0.09	
	Δ VV (op)	-0.73 ± 0.02	-0.55 ± 0.01	0.12 ± 0.01	-0.39 ± 0.005	-0.03 ± 0.02

545 Δ - pre- to post-fire temporal differences of VV and VH backscatter data by pixels classes of: burned (bp) and
546 commission (cp) and omission (oe) errors.

547 For six of the validation sites, images from ascending and descending Sentinel-1 passes were available. Therefore,
548 a more detailed analysis was carried out to understand the difference in BA accuracy between ascending and descend-
549 ing passes (Fig. 9). Overall, BA omission errors were minimum when both passes were used while BA commission

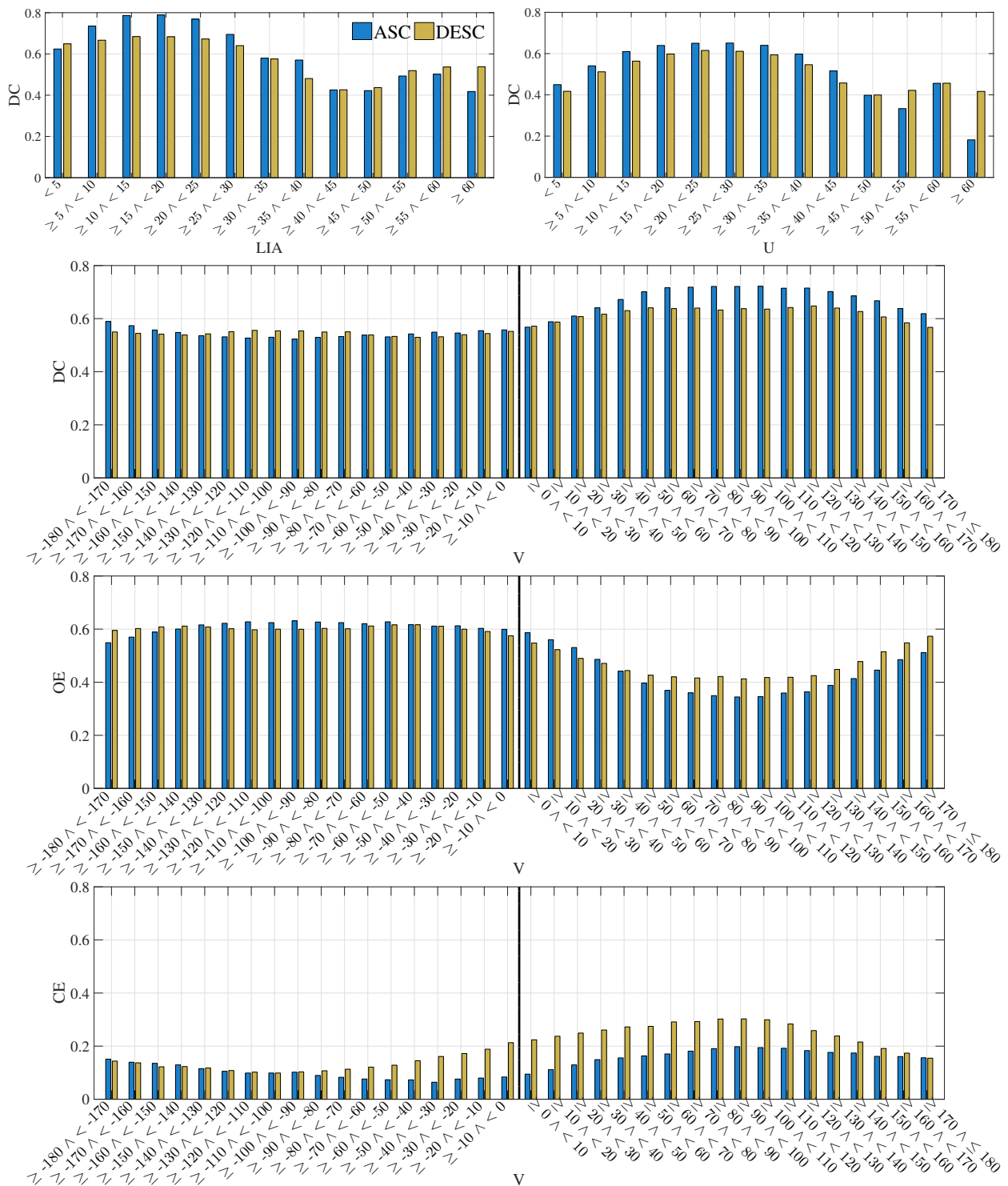
550 errors increased. However, DC values showed that BA detection generally improved when data from both passes was
 551 available.



552
 553 Fig. 9: Assessment metrics of Sentinel-1 burned area detections per ascending (A), descending (D) and both satellite passes (B). DC - Dice
 554 coefficient, OE - omission error and CE - commission error.
 555

557 The effect of topography and the environmental conditions (soil moisture) were analysed for each acquisition pass
 558 over the six tiles. The LIA was often used to analyse the effect of topography on the backscatter coefficient in areas
 559 affected by fires (Tanase et al., 2009, 2010a; Kalogirou et al., 2014; Gimeno & San-Miguel-Ayanz, 2004; Kurum,
 560 2015). However, the wide swath of the Sentinel-1 IW mode results in a variation of the incidence angle of about 17°
 561 from near (29°) to far (46°) range. Since LIA is a function of incidence angle and local slope (U), DC scores were
 562 analysed (by satellite pass) as a function of both angles after grouping in five degrees classes (Tanase et al., 2010a).
 563 Similar trends were observed for both passes (Fig. 10) with better accuracies being observed for low LIAs and Us
 564 groups (<40°).

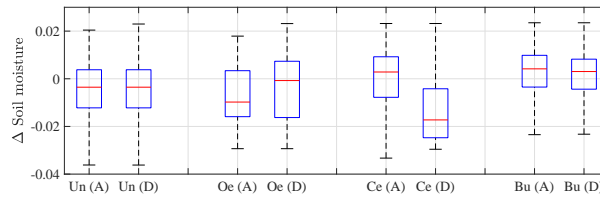
565 Nevertheless, analysing BA accuracy by LIA and U angles has limitations as LIA groups may include areas of dif-
 566 ferent slopes while U groups may include slopes oriented towards and away from the sensor with completely different
 567 scattering properties. Therefore, the sloped areas (U≥5°) were further analysed by their orientation (V) with respect
 568 to the satellite viewing geometry (Fig. 10). Notice that positive V values are observed for slopes oriented towards the
 569 sensor while negative values are observed for slopes oriented away from the sensor. The BA accuracy improved over
 570 pixels oriented toward the sensor with omission error being lower for such pixels while commission errors slightly
 571 higher. Notice that a paired t-test showed no significant difference (p-value > 0.05) between the percentage of pixels
 572 (by ten degrees V groups) from ascending and descending satellite passes.



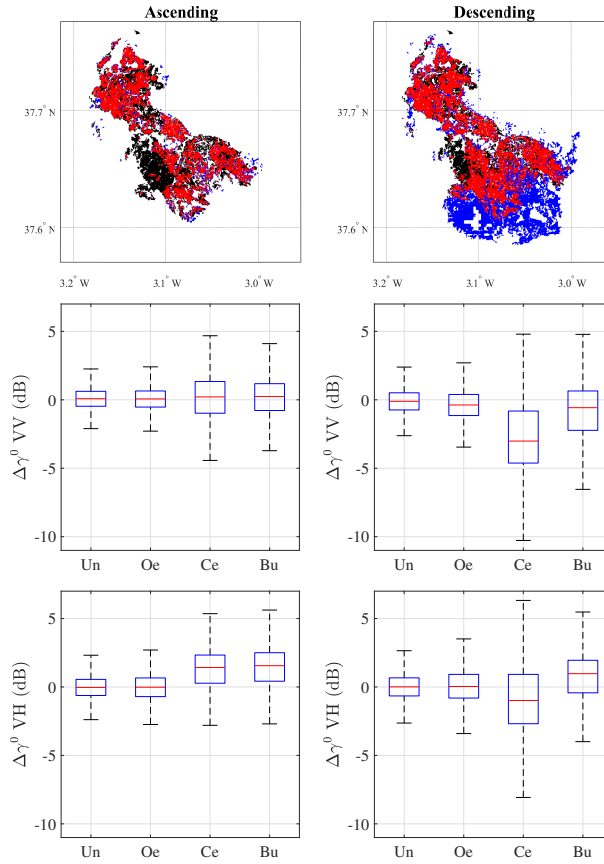
573

574 Fig. 10: Dice coefficient (DC) by local incidence angle (LIA) and local slope (U) groups. For sloped areas ($U \geq 5^\circ$ degrees) the DC, commission
 575 (CE) and omission errors (OE) are shown as a function of slope orientation (V) with respect to the Sentinel-1 viewing geometry. Negative V values
 576 show slopes oriented away the sensor while positive V values show slopes oriented toward the sensor. The BA metrics are shown for six tiles where
 577 both ascending (ASC) and descending (DESC) passes were available (i.e., 10SEH, 10UEC, 29TNE, 29TNG, 30SVG and 30TYK).
 578

580 Since Sentinel-1 ascending and descending images were acquired at different dates, variations in soil moisture
 581 (from the global SMAP product) between the pre- and post-dates delineating the CDPs were analysed to ascertain the
 582 influence of this important environmental parameter on BA detection errors. Over five of the six tiles the difference
 583 in soil moisture between ascending and descending passes were reduced. However, for tile 30SVG soil moisture
 584 increased considerably over some areas for descending pass acquisitions which translated in much larger commission
 585 errors (0.46) when compared to those observed for the ascending pass (0.16), where soil moisture was stable (Fig. 11).
 586 The increased commission errors were the result of a large and compact area located south of the fire perimeter that
 587 was misclassified as burned (Fig. 12). The temporal variations of the backscatter coefficient between ascending and
 588 descending passes (tile 30SVG) were correlated with the accuracy metrics. An important variation of the backscatter
 589 coefficient during the descending pass was observed over the misclassified burned area (CE) for both VV (2.8 ± 0.029)
 590 and VH (1.0 ± 0.027) polarizations (Fig. 12).



591
 592 Fig. 11: Temporal variations of soil moisture (SM) from Soil Moisture Active Passive (SMAP) mission for pre- and post-fire dates ($\Delta_{SM} =$
 593 $SM_{pre} - SM_{post}$), in tile 30SVG. Ascending (A) and descending (D) passes are analyzed separately. Pixels are grouped by classes of unburned (Un)
 594 and burned (Bu). Pixels from areas affected by commission (Ce) and omission errors (Oe) are also shown. The red line indicates median value, and
 595 top and bottom box edges indicate the 75th and respectively the 25th percentiles. Outliers are not shown to improve graph discernibility.
 596



598

599 Fig. 12: Burned area from ascending (left column) and descending (right column) passes in tile 30SVG: red – burned (Bu), white – unburned (Un),
600 black – omission errors (Oe) and blue – commission errors (Ce). VV and VH backscatter coefficient variation ($\Delta\gamma^0 = pre_{fire} - post_{fire}$) is also
601 shown for each pass.
602

604 5. Discussion

605 5.1. Algorithm development

606 The Reed-Xiaoli anomaly detector (Reed & Yu, 1990), not widely used with SAR images except for levee slide
607 detection (Dabbiru et al., 2012, 2016, 2018), seemed to work coherently when detecting burned areas as errors of
608 omission appeared when low backscatter changes were observed over burned areas while error of commissions ap-
609 peared due to fire unrelated backscatter variations over unburned areas. These trends were reflected by the MAC
610 values for OE and CE classes which were close to those observed for unburned and respectively burned areas sug-
611 gesting a correct estimation of the covariance matrices by taking advantage of the *a priori* information from stable
612 areas (i.e., likely unburned pixels). Comparing backscatter variability over burned and unburned classes one may
613 notice notably smaller MAC values over the later which also suggests a properly functioning of the anomaly detector
614 according to the input data. To test the correct delineation of stable areas (i.e., background), a t-test was used to
615 analyse the statistical difference between the inverted covariance matrices (used by RXD) obtained using hotspots and

616 those obtained using the BA validation perimeters from optical data (section 3.4). The analysis showed no statistical
617 difference (p-values > 0.05) between the two methods demonstrating that hotspots may be reliably used to identify
618 likely burned and unburned pixels as a preliminary source of burned area.

619 The use of ancillary information from thermal anomalies (hotspots) allowed for attributing anomalous changes
620 of SAR backscatter data as BA through a locally derived knowledge extraction. Hence, burned pixels were extracted
621 without the need for relying on fixed thresholds on the SAR signal, which may depend not only on the land cover
622 type, but also on backscatter variations due to spatially variable influencing factors (e.g., soil and vegetation moisture)
623 that are difficult to model. Temporal decorrelation between hotspots (i.e., fire date) and the date at which radar
624 backscatter changes were detected (Belenguer-Plomer et al., 2018b) was observed over most tiles. One should notice
625 that temporal decorrelation is not specific to burned area nor the C-band frequency as similar effects were observed
626 for L-band HV polarization over areas affected by deforestation (Watanabe et al., 2018). Therefore, temporal studies
627 using SAR-based change detection techniques must devise methods to reduce or account for such effects (see the
628 proposed approach in the Stage 3).

629 The use of a non-parametric classifier was essential to cope with the temporal lack of hotspots due to persistent cloud
630 cover or small fire size (i.e., not detected by thermal sensors). Parametrising random forests classifier (RF) for BA
631 classification may prove complex as almost an infinite combinations of parameter settings are possible. Ramo &
632 Chuvieco (2017) proposed using 600 trees and a stratified training, where 10% of training data were burned pixels
633 and the rest not burned, for the classification of MODIS images in burned and unburned classes. Such a setting was
634 tested during algorithm development but the results were not as accurate as expected. Therefore, the RF set-up was
635 customized based on empirical observations. The substantial differences in RF parametrization settings were mainly
636 caused by the algorithm design, since it is building specific RF models for each land cover type and detection period.
637 Hence, it does not have to cope with widely varying land cover and burn conditions as the work of Ramo & Chuvieco
638 (2017) which used one uniquely trained model worldwide.

639 5.2. Comparison with global products

640 Over most validation areas, the accuracy of the proposed algorithm was higher when compared to the MCD64A1
641 Version 6 product (Giglio et al., 2018). The mean DC value over all studied locations was 0.13 higher for the Sentinel-
642 1 BA detections (i.e., 28% higher). The DC values of Sentinel-1 detections per tiles were statistically higher than those
643 of MCD64A1 (paired t-test p-value of 0.024). In addition, the variability of Sentinel-1 BA detection accuracy was
644 considerably lower when compared to the MCD64A1 product. The mean values for OE and CE over all tiles were
645 also lower for the Sentinel-1 detections.

646 The analysis showed that for 13 tiles (72% of the studied areas) the Sentinel-1 BA detections had higher DC scores
647 than the MCD64A1 product. For one tile, 33NUF, the difference in accuracy (DC) of the two products is 0.5. The
648 very low accuracy (DC 0.02) observed over this tile for the MCD64A1 product is difficult to explain with the data at
649 hand, hence the tile was considered an outlier. For five tiles (i.e., 18NXG, 30TYK, 33NTG, 33NUG, and 49MHT)

650 the improvement of the Sentinel-1 product was substantial with DC increasing on average by 144% when compared
651 to the MCD64A1 product. The large difference in DC scores was mainly caused by the high OE (0.72 to 0.94) in
652 the MCD64A1 product. Detection of small burned areas (< 120 ha) is problematic using MODIS data due to the
653 coarse sensor resolution (Giglio et al., 2009). To evaluate if reduced spatial resolution of MODIS was the reason
654 behind MCD64A1 product poor performance, the percentage of BA from fire scars below 120 ha was computed
655 based on the reference datasets. In tiles 33NUG, 33NTG, and 49MHT fires below 120 ha constituted 85%, 53% and
656 respectively 48% of the total BA suggesting that the lower performance may be related to the coarser MODIS spatial
657 resolution. Therefore, these results suggest that improvements in BA detection accuracy may be possible not only in
658 areas with frequent cloud cover. However, for tiles 18NXG and 30TYK small fires (< 120 ha) constituted only 34%
659 and respectively 25% of the total BA indicating that fire size may not be the only factor influencing detection accuracy
660 when using coarse resolution sensors.

661 For five tiles (i.e., 29TNE, 30SVG, 36NXP, 48VWL and 50JML) the MCD64A1 product showed higher DC scores
662 when compared to the Sentinel-1 based detections. The mean difference for the four first tiles was only 0.13. However,
663 for tile 50JML this difference was higher, with the MCD64A1 product being markedly more accurate (DC 0.41 vs.
664 0.21). It seems such large differences were related to the conditions encountered over the Australian grasslands, where
665 backscatter variations recorded from pre- to post-fire periods were low, hindering the detection algorithm. By land
666 cover class, the results indicate that a radar-based BA mapping algorithm may provide BA products with better or
667 similar accuracies when compared to available global products, except for grasslands. The most significant difference
668 in accuracy was observed over grasslands, where the MCD64A1 was more accurate than the Sentinel-1 based BA (DC
669 0.45 vs. 0.28). Conversely, over forests Sentinel-1 derived BA was more accurate (DC 0.64 vs. 0.49).

670 5.3. Factors influencing BA accuracy

671 Temporal variation of pre- and post-fire VH and VV backscatter coefficient over pixels of affected by CE and OE
672 were similar to those observed over burned and respectively unburned pixels. Following, the main factors affecting
673 burned area classification were discussed.

674 5.3.1. Environmental conditions

675 CE may only be related to factors that modify the scattering properties in a similar manner to fires (~~e.g., rainfall,~~
676 ~~harvest, defoliation, snow-melt, logging~~) if backscatter changes are concentrated in a reduced part of the image
677 (anomalous changes), since the RXD may identify such variations as spatial anomalies similar than fires. For in-
678 stance, unrelated fire backscatter variations which did not affect the entire image occurred over tile 30SVG, where the
679 highest difference between commission errors for ascending (0.16) and descending (0.46) passes were observed. For
680 this tile, soil moisture variations over CE pixels varied notably between ascending and descending passes. For the
681 descending pass, post-fire soil moisture was on average $0.014 \pm 1.18e-04 \text{ m}^3/\text{m}^3$ higher when compared to pre-fire
682 soil moisture, while for the ascending pass the increment was marginal ($6.2e-04 \text{ m}^3/\text{m}^3$). Consequently, over pixels

683 affected by CE, an average increase of 2.8 ± 0.029 dB for VV polarization and 1.0 ± 0.027 dB for the VH polarization
684 was recorded from pre- to post-fire date for the descending acquisitions. The differentiated increase by polarization
685 confirmed the larger influence of the soil surface properties on the VV polarization when compared to the VH polar-
686 ization as noted previously by others authors (Freeman & Durden, 1998; Yamaguchi et al., 2005; Van Zyl et al., 2011).
687 The backscatter coefficient change generated by variations in soil moisture was incorrectly mapped as burned since:
688 (i) the algorithm does not account for the sign of the backscatter change; and (ii) the image part affected by rainfall
689 was located close to hotspots (areas bordering the fire perimeter). This suggests that algorithm improvements may
690 further mitigate commission errors related to soil moisture variations by considering the backscatter change direction.
691 Notice that, tile 30SVG was an exception as at this location a major part (67.6%) of the CE were concentrated in an
692 large enough area (3420 ha) to extract useful information from the coarse pixel spacing SMAP product. The influence
693 of soil moisture on BA accuracy was inconclusive for rest of the tiles, most probably due to the coarse pixel spacing
694 of the SMAP product (9 km). ~~Since global products of snow-melt,~~ The use of soil moisture products at higher spatial
695 resolution, such as the Copernicus Surface Soil Moisture (SSM) based on Sentinel-1 data at 1 km of pixel spacing
696 (Bauer-Marschallinger et al., 2018), to reduce CE derived from soil moisture variations will be investigated when
697 global available, since now exists only for Europe. On the other hand, since global products of harvest, defoliation,
698 floods or logging at enough detailed pixel spacing are not available and precipitation products based on extrapolation
699 of data from rain gauges have a much coarser pixel spacing (0.5°) and own errors (Hu et al., 2018), it was not possible
700 to identify all the commission errors sources in order to filter them.

701 5.3.2. Fire impact

702 Conversely, pixels affected by OE may have been the result of the effects of different variables which attenuated
703 the vegetation combustion effects on the C-band backscatter coefficient. Fire severity, the degree of organic matter
704 loss due to fire combustion (Keeley, 2009), constrains the temporal backscatter variation between pre- and post-fire
705 (Tanase et al., 2010b, 2014). The dNBR mean values over the pixels affected by omission errors ($0.068 \pm 6.65e-05$)
706 was 22.73% lower when compared to the dNBR values observed for correctly detected burned pixels ($0.088 \pm 7.5e-$
707 05). Notice that the dNBR index is widely used to detect BA and estimate fire severity over a range of biomes (Escuin
708 et al., 2008; Loboda et al., 2007; Van Wagtenonk et al., 2004; Tanase et al., 2011) and that high fire severity implies
709 a more significant reduction of vegetated scattering elements due to combustion.

710 5.3.3. Topography

711 Topography also affected the BA accuracy, with a tendency of increased burned areas omission being observed for
712 the pixels oriented away from the sensor most likely due to the existence of shadowed regions (Tanase et al., 2010a,
713 2009). Conversely, for the pixels oriented towards the sensor the commission errors increased since soil proprieties had
714 a higher influence on radar scattering. Since the OE derived of the topography were higher than the CE, to improve the
715 BA accuracy, detections from different relative orbits were joined when available (see subsection 5.3.5). The angle

716 of incidence determines the accuracy not also in SAR based fire monitoring, since in Xu et al. (2019) it is observed
717 how also affects the land cover classification accuracy.

718 5.3.4. Land cover type

719 The variables mentioned above affect the scattering processes over burned and unburned areas differently depend-
720 ing of the land cover class observed and translated into variable map accuracies. Lower BA accuracies were found
721 over grasslands as the scattering elements characteristic for this vegetation type interact to a lesser extent with the C-
722 band waves when compared to the scattering elements encountered in shrubs and forests (stems, branches). However,
723 the most important factor affecting the algorithm sensitivity to fire in grasslands seemed to be related to fire timing. In
724 areas characterized by long intervals (months) between grass curing and fire events the algorithm encountered diffi-
725 culties as the cured (i.e., dry) grass has low scattering properties being mostly transparent to the radar waves (Menges
726 et al., 2004). Therefore, grass consumption by fire results in small or nil VV and VH backscatter changes from vegeta-
727 tion consumption which hinders BA detection. This observation seemed supported by the lower temporal variation of
728 the backscatter coefficient over burned when compared unburned grasslands. Conversely, forest and shrubs, besides
729 containing scattering elements more susceptible to interact to C-band radar waves, are not affected by curing to the
730 same extent (i.e., some water needs to be retained to ensure plant survival). Thus, vegetation consumption by fire
731 results in a noticeable scattering decrease which is detected by the algorithm, although sometimes a temporal gap
732 between fire and detection was observed (temporal decorrelation) as discussed in Belenguer-Plomer et al. (2018b).

733 5.3.5. Ancillary information and SAR data availability

734 The use of hotspots was essential given that only two backscatter channels were available (VV and VH polar-
735 izations). Without hotspots, differentiation of burned areas from other land changes (e.g., floods, logging, harvest,
736 vegetation disturbance due to pests, drought) that modulate the backscatter coefficient in a similar fashion was diffi-
737 cult as also noted by Huang & Siegert (2006). Lower BA detection accuracies were found in pixels located far (outside
738 IAhs) when compared to pixels located in close proximity (within 750 m) of hotspots events (see supplementary ma-
739 terial). According to the reference data, only a 15.3% of burned pixels were not located within IAhs allowing for BA
740 detection rates comparable or better than those of currently available global products.

741 Joining detections from different ~~passes~~ (relative orbits (from ascending and descending passes)) increased the
742 detected burned area. Inherently, the availability of several orbits covering the same area resulted in reduced OE which
743 is particularly true when different viewing geometries were used over areas with steep topography. Conversely the CE
744 increased as wrongly detected areas are also joined in post-processing (Stage 5 of the algorithm). Despite the increased
745 CEs, the use of both Sentinel-1 passes generally improved the BA accuracy. It should be noted that consistent dual
746 pass (ascending and descending) acquisitions are currently available only over Europe and North America. The
747 analysis suggested that differences in BA accuracy between ascending and descending passes were mainly caused
748 by the interaction between the viewing geometry and the local topography as explained in subsection 4.3, with the

749 highest accuracies being achieved over areas oriented towards the sensor. Using images acquired in a single pass
750 may result in increased omission errors particularly in regions with accentuated topography. These results confirm
751 previous findings that highlight the effect of topography on burned area detection and fire impact estimation (Gimeno
752 & San-Miguel-Ayanz, 2004; Huang & Siegert, 2006; Tanase et al., 2010b). Future investigations in order to reduce
753 topographic effects will be needed, since according to current Sentinel-1 observation scenario, over most of Earth
754 surface data is taken only in a single pass.

755 The accuracy of the Sentinel-1 product was also assessed as a function of the number of SAR images available
756 during the detection period as well as the number of days between consecutive acquisitions. The BA was detected
757 regardless of the image number or their temporal distance, thus coping with the variable acquisition strategy (temporal
758 frequency) of the Sentinel-1 mission over different regions. The main temporal factor which limited the algorithm
759 accuracy was the post-fire vegetation regrowth cycle. Where image acquisitions were more frequent, when compared
760 to vegetation regrowth cycles, the algorithm detected the changes in backscatter coefficient generated by fires and
761 labelled them as BA. However, the relationship between BA detection accuracy (DC) and the number of images used
762 and their acquisition frequency (day difference of consecutive images) per tiles was weak (0.32 and respectively 0.38
763 Pearson's correlation coefficient) since additional factors affected the algorithm accuracy (i.e., topography and fire
764 unrelated changes). Thus, it was concluded that current Sentinel-1 temporal frequencies might be sufficient for global
765 retrieval. Nevertheless, the relatively small number of test samples may have obscured some effects. In addition, the
766 relationship between Sentinel-1 acquisition frequency and the detection accuracy may vary with the land cover type
767 (different post-fire regrowth cycle).

768 5.4. Comparison with previous Sentinel-1 based approaches

769 Previous studies based on Sentinel-1 data for BA detection were carried out only at local to regional scales.
770 However, C-band backscatter from fire affected areas varies with the local conditions. Therefore, locally trained
771 algorithms are difficult to transfer to other regions. Engelbrecht et al. (2017) used empirical thresholds to detect BA
772 in South Africa achieving OE and CE of 0.29 and 0.48, respectively. Depending on area, the proposed algorithm may
773 achieve similar or better accuracies. Lohberger et al. (2018) used an object-based image analysis approach to detect
774 BA in Indonesia. However, since only information on the overall accuracy was provided comparisons were difficult.
775 Finally, Verhegghen et al. (2016) tested the most suitable thresholds when separating burned from unburned pixels in
776 the Congo basin, but did not provide accuracy metrics of their detected BA. Nevertheless, since such studies relied
777 on algorithms heavily optimized over local to regional scales, comparisons with the proposed algorithm are of little
778 relevance.

779 6. Conclusions

780 This paper introduced an automated and cloud cover insensitive algorithm for BA detection using Sentinel-1
781 dual-polarized backscatter images. Hotspots from active fires and land cover data were used as ancillary information

782 when attributing anomalous backscatter changes to burned and unburned classes. The algorithm was validated at
783 18 locations (100×100 km tiles) covering over 21 million hectares worldwide. Algorithm accuracy was assessed
784 using reference burn perimeters derived from optical sensors (Landsat-8 and Sentinel-2). The agreement between the
785 Sentinel-1 algorithm and the reference perimeters was compared with that of the most widely used global BA product,
786 the MCD64A1 Version 6. Over all tiles, the mean OE and CE for BA were 0.43 and 0.37, respectively. The mean DC
787 was 0.59. When compared with the MCD64A1, the proposed algorithm improved burned area detection (DC) by 28%
788 (from 0.46 to 0.59) over the analysed tiles. This improvement was mainly related to ~~reduced OE~~ reduce OE, which is
789 very useful for the users, since has been demonstrated that Sentinel-1 may be a key source of information, especially
790 where optical data based products have information gaps, due mainly to clouds.

791 According to our analysis, strong topography conditioned the BA accuracy with slopes oriented away from the
792 sensor being subject to higher errors, being necessary combine detections from different relative orbits to cope these
793 effects. Likewise, it was observed that a reduced fire severity translated into increased omission errors. On the other
794 hand, commission errors seemed to correlate with fire unrelated changes affecting the scattering processes (~~e.g.,~~
795 ~~soil moisture~~). Furthermore, scattering from burned areas was directly influenced by vegetation type with higher
796 accuracies being observed over forested areas (DC 0.64) and lower over grasslands (DC 0.28) which were attributed
797 to the difficulty in tracking changes of cured vegetation using the C-band data. The main advantages of the proposed
798 algorithm were related to: (i) ~~insensitivity to cloud cover;~~ Self-adapting to local scattering conditions to extract
799 burned area without the need of fixed thresholds or prior information of observed area; and (ii) ~~independence between~~
800 ~~accuracy and Sentinel-1 temporal frequency; and~~ (iii) ~~more detailed pixel spacing when compared to current global~~
801 ~~products~~ capability of BA detection when thermal anomalies were not available using random forests models built
802 from data when were available. On the other hand, the main limitations were related to the: (i) misclassification of
803 fire unrelated changes (~~e.g., due to soil moisture~~); (ii) positive relationship between accuracy and hotspots availability;
804 and (iii) accuracy dependence on variables affecting radar scattering processes (e.g., ecosystem type, topography). To
805 reduce such limitations, further improvements shall be investigated.

806 Acknowledgements

807 This work has been financed by the European Space Agency through the Phase 2 of the Fire_cci (Climate Change
808 Initiative) project (Contract 4000115006/15/I-NB) and by the Spanish Ministry of Science, Innovation and Univer-
809 sities through a FPU doctoral fellowship (FPU16/01645). We acknowledge the use of data from LANCE FIRMS
810 operated by the NASA GSFC Earth Science Data and Information System (ESDIS). We also acknowledge Dr. Thierry
811 Koleck and Dr. Stephane Mermoz for kindly providing the code for Sentinel-1 data pre-processing and the comments
812 and suggestions of several anonymous reviewers which helped improving the original manuscript.

813 **References**

- 814 Alonso-Canas, I., & Chuvieco, E. (2015). Global burned area mapping from ENVISAT-MERIS and MODIS active fire data. *Remote Sensing of*
815 *Environment*, *163*, 140–152.
- 816 Andela, N., Morton, D., Giglio, L., Chen, Y., Van Der Werf, G., Kasibhatla, P., DeFries, R., Collatz, G., Hantson, S., Kloster, S. et al. (2017). A
817 human-driven decline in global burned area. *Science*, *356*, 1356–1362.
- 818 Andreae, M. O., & Merlet, P. (2001). Emission of trace gases and aerosols from biomass burning. *Global Biogeochemical Cycles*, *15*, 955–966.
- 819 Antikidis, E., Arino, O., Arnaud, A., & Laur, H. (1998). ERS SAR Coherence & ATSR Hot Spots: a Synergy for Mapping Deforested Areas. The
820 Special Case of the 1997 Fire Event in Indonesia. *European Space Agency-Publications-ESA SP*, *441*, 355–360.
- 821 Aponte, C., de Groot, W. J., & Wotton, B. M. (2016). Forest fires and climate change: causes, consequences and management options. *International*
822 *Journal of Wildland Fire*, *25*, i–ii.
- 823 Banerjee, A., Burlina, P., & Diehl, C. (2006). A support vector method for anomaly detection in hyperspectral imagery. *IEEE Transactions on*
824 *Geoscience and Remote Sensing*, *44*, 2282–2291.
- 825 Bastarrika, A., Chuvieco, E., & Martín, M. P. (2011). Mapping burned areas from Landsat TM/ETM+ data with a two-phase algorithm: Balancing
826 omission and commission errors. *Remote Sensing of Environment*, *115*, 1003–1012.
- 827 Bauer-Marschallinger, B., Freeman, V., Cao, S., Paulik, C., Schaufler, S., Stachl, T., Modanesi, S., Massari, C., Ciabatta, L., Brocca, L. et al. (2018).
828 Toward Global Soil Moisture Monitoring With Sentinel-1: Harnessing Assets and Overcoming Obstacles. *IEEE Transactions on Geoscience*
829 *and Remote Sensing*, (pp. 1–20).
- 830 Belenguer-Plomer, M. A., Tanase, M. A., Fernandez-Carrillo, A., & Chuvieco, E. (2018a). Insights into burned areas detection from Sentinel-1 data
831 and locally adaptive algorithms. In *Active and Passive Microwave Remote Sensing for Environmental Monitoring II* (p. 107880G). International
832 Society for Optics and Photonics volume 10788.
- 833 Belenguer-Plomer, M. A., Tanase, M. A., Fernandez-Carrillo, A., & Chuvieco, E. (2018b). Temporal backscattering coefficient decorrelation in
834 burned areas. In *Active and Passive Microwave Remote Sensing for Environmental Monitoring II* (p. 107880T). International Society for Optics
835 and Photonics volume 10788.
- 836 Belgiu, M., & Drăguț, L. (2016). Random forest in remote sensing: A review of applications and future directions. *ISPRS Journal of Photogram-*
837 *metry and Remote Sensing*, *114*, 24–31.
- 838 Bojinski, S., Verstraete, M., Peterson, T. C., Richter, C., Simmons, A., & Zemp, M. (2014). The concept of essential climate variables in support
839 of climate research, applications, and policy. *Bulletin of the American Meteorological Society*, *95*, 1431–1443.
- 840 Bond, W. J., Woodward, F. I., & Midgley, G. F. (2005). The global distribution of ecosystems in a world without fire. *New Phytologist*, *165*,
841 525–538.
- 842 Boschetti, L., Flasse, S. P., & Brivio, P. A. (2004). Analysis of the conflict between omission and commission in low spatial resolution dichotomic
843 thematic products: The Pareto Boundary. *Remote Sensing of Environment*, *91*, 280–292.
- 844 Boschetti, L., Roy, D. P., Justice, C. O., & Giglio, L. (2010). Global assessment of the temporal reporting accuracy and precision of the MODIS
845 burned area product. *International Journal of Wildland Fire*, *19*, 705–709.
- 846 Bourgeau-Chavez, L., Harrell, P., Kasischke, E., & French, N. (1997). The detection and mapping of Alaskan wildfires using a spaceborne imaging
847 radar system. *International Journal of Remote Sensing*, *18*, 355–373.
- 848 Bourgeau-Chavez, L., Kasischke, E., Brunzell, S., Mudd, J., & Tukman, M. (2002). Mapping fire scars in global boreal forests using imaging radar
849 data. *International Journal of Remote Sensing*, *23*, 4211–4234.
- 850 Bowman, D. M., Balch, J. K., Artaxo, P., Bond, W. J., Carlson, J. M., Cochrane, M. A., D’Antonio, C. M., DeFries, R. S., Doyle, J. C., Harrison,
851 S. P. et al. (2009). Fire in the Earth system. *Science*, *324*, 481–484.
- 852 Bradley, A. V., Tansey, K., & Chuvieco, E. (2012). The ESA climate change initiative: Merging burned area estimates for the Fire Essential Climate
853 Variable. In *Geoscience and Remote Sensing Symposium (IGARSS), 2012 IEEE International* (pp. 7153–7156). IEEE.
- 854 Breiman, L. (2001). Random forests. *Machine learning*, *45*, 5–32.

- 855 Chan, S. (2016). Enhanced Level 3 Passive Soil Moisture Product Specification Document. Jet Propulsion Lab., California Inst. Technol.: Pasadena,
856 CA, USA.
- 857 Chan, S., Bindlish, R., O'Neill, P., Jackson, T., Njoku, E., Dunbar, S., Chaubell, J., Piepmeier, J., Yueh, S., Entekhabi, D. et al. (2018). Development
858 and assessment of the SMAP enhanced passive soil moisture product. *Remote sensing of environment*, 204, 931–941.
- 859 Chawla, N. V., Bowyer, K. W., Hall, L. O., & Kegelmeyer, W. P. (2002). SMOTE: Synthetic Minority Over-sampling Technique. *Journal of*
860 *Artificial Intelligence Research*, 16, 321–357.
- 861 Chen, C., Liaw, A., & Breiman, L. (2004). Using random forest to learn imbalanced data. *University of California, Berkeley*, 110.
- 862 Chen, Q., Zeng, J., Cui, C., Li, Z., Chen, K.-S., Bai, X., & Xu, J. (2018). Soil moisture retrieval from smap: A validation and error analysis study
863 using ground-based observations over the little washita watershed. *IEEE Transactions on Geoscience and Remote Sensing*, 56, 1394–1408.
- 864 Chuvieco, E., Lizundia-Loiola, J., Pettinari, M. L., Ramo, R., Padilla, M., Mouillot, F., Laurent, P., Storm, T., Heil, A., & Plummer, S. (2018).
865 Generation and analysis of a new global burned area product based on MODIS 250m reflectance bands and thermal anomalies. *Earth Syst. Sci.*
866 *Data Discuss*, 512, 1–24.
- 867 Chuvieco, E., Yue, C., Heil, A., Mouillot, F., Alonso-Canas, I., Padilla, M., Pereira, J. M., Oom, D., & Tansey, K. (2016). A new global burned
868 area product for climate assessment of fire impacts. *Global Ecology and Biogeography*, 25, 619–629.
- 869 Collins, L., Griffioen, P., Newell, G., & Mellor, A. (2018). The utility of random forests for wildfire severity mapping. *Remote Sensing of*
870 *Environment*, 216, 374–384.
- 871 Dabbiru, L., Aanstoos, J. V., Ball, J. E., & Younan, N. H. (2018). Machine Learning Framework for Mapping of Mississippi River Levees and
872 Damage Assessment Using Terrasar-X Data. In *IGARSS 2018-2018 IEEE International Geoscience and Remote Sensing Symposium* (pp.
873 5855–5858). IEEE.
- 874 Dabbiru, L., Aanstoos, J. V., Mahrooghy, M., Li, W., Shanker, A., & Younan, N. H. (2012). Levee anomaly detection using polarimetric synthetic
875 aperture radar data. In *Geoscience and Remote Sensing Symposium (IGARSS), 2012 IEEE International* (pp. 5113–5116). IEEE.
- 876 Dabbiru, L., Aanstoos, J. V., & Younan, N. H. (2016). Earthen levee slide detection via automated analysis of synthetic aperture radar imagery.
877 *Landslides*, 13, 643–652.
- 878 Di Gregorio, A. (2005). *Land Cover Classification System: Classification Concepts and User manual*. United Nations Food and Agriculture
879 Organization.
- 880 Du, P., Samat, A., Waske, B., Liu, S., & Li, Z. (2015). Random forest and rotation forest for fully polarized SAR image classification using
881 polarimetric and spatial features. *ISPRS Journal of Photogrammetry and Remote Sensing*, 105, 38–53.
- 882 Engelbrecht, J., Theron, A., Vhengani, L., & Kemp, J. (2017). A simple normalized difference approach to burnt area mapping using multi-
883 polarisation C-Band SAR. *Remote Sensing*, 9, 764.
- 884 Escuin, S., Navarro, R., & Fernandez, P. (2008). Fire severity assessment by using NBR (Normalized Burn Ratio) and NDVI (Normalized
885 Difference Vegetation Index) derived from LANDSAT TM/ETM images. *International Journal of Remote Sensing*, 29, 1053–1073.
- 886 Eva, H., & Lambin, E. F. (1998). Remote sensing of biomass burning in tropical regions: sampling issues and multisensor approach. *Remote*
887 *Sensing of Environment*, 64, 292–315.
- 888 Fernandez-Carrillo, A., Belenguier-Plomer, M., Chuvieco, E., & Tanase, M. (2018). Effects of sample size on burned areas accuracy estimates in
889 the Amazon Basin. In *Earth Resources and Environmental Remote Sensing/GIS Applications IX* (p. 107901S). International Society for Optics
890 and Photonics volume 10790.
- 891 Flannigan, M. D., Amiro, B. D., Logan, K. A., Stocks, B., & Wotton, B. (2006). Forest fires and climate change in the 21 st century. *Mitigation*
892 *and Adaptation Strategies for Global Change*, 11, 847–859.
- 893 Flannigan, M. D., Krawchuk, M. A., de Groot, W. J., Wotton, B. M., & Gowman, L. M. (2009). Implications of changing climate for global
894 wildland fire. *International Journal of Wildland Fire*, 18, 483–507.
- 895 Freeman, A., & Durden, S. L. (1998). A three-component scattering model for polarimetric SAR data. *IEEE Transactions on Geoscience and*
896 *Remote Sensing*, 36, 963–973.
- 897 French, N. H., Bourgeau-Chavez, L. L., Wang, Y., & Kasischke, E. S. (1999). Initial observations of Radarsat imagery at fire-disturbed sites in

898 interior Alaska. *Remote Sensing of Environment*, 68, 89–94.

899 Frey, O., Santoro, M., Werner, C. L., & Wegmuller, U. (2013). DEM-based SAR pixel-area estimation for enhanced geocoding refinement and
900 radiometric normalization. *IEEE Geoscience and Remote Sensing Letters*, 10, 48–52.

901 García, M. L., & Caselles, V. (1991). Mapping burns and natural reforestation using Thematic Mapper data. *Geocarto International*, 6, 31–37.

902 Giglio, L., Boschetti, L., Roy, D. P., Humber, M. L., & Justice, C. O. (2018). The Collection 6 MODIS burned area mapping algorithm and product.
903 *Remote sensing of environment*, 217, 72–85.

904 Giglio, L., Descloitres, J., Justice, C. O., & Kaufman, Y. J. (2003). An enhanced contextual fire detection algorithm for MODIS. *Remote Sensing
905 of Environment*, 87, 273–282.

906 Giglio, L., Loboda, T., Roy, D. P., Quayle, B., & Justice, C. O. (2009). An active-fire based burned area mapping algorithm for the MODIS sensor.
907 *Remote Sensing of Environment*, 113, 408–420.

908 Gimeno, M., San-Miguel, J., Barbosa, P., & Schmuck, G. (2002). Using ERS-SAR images for burnt area mapping in Mediterranean landscapes.
909 *Forest Fire Research & Wildland Fire Safety*. (Viegas T ed). Millpress, Rotterdam, 90.

910 Gimeno, M., & San-Miguel-Ayanz, J. (2004). Evaluation of RADARSAT-1 data for identification of burnt areas in Southern Europe. *Remote
911 Sensing of Environment*, 92, 370–375.

912 Gimeno, M., San-Miguel-Ayanz, J., & Schmuck, G. (2004). Identification of burnt areas in Mediterranean forest environments from ERS-2 SAR
913 time series. *International Journal of Remote Sensing*, 25, 4873–4888.

914 Gislason, P. O., Benediktsson, J. A., & Sveinsson, J. R. (2006). Random forests for land cover classification. *Pattern Recognition Letters*, 27,
915 294–300.

916 Hansen, M. C., Potapov, P. V., Moore, R., Hancher, M., Turubanova, S., Tyukavina, A., Thau, D., Stehman, S., Goetz, S., Loveland, T. et al. (2013).
917 High-resolution global maps of 21st-century forest cover change. *Science*, 342, 850–853.

918 Hoffmann, W. A., Schroeder, W., & Jackson, R. B. (2002). Positive feedbacks of fire, climate, and vegetation and the conversion of tropical
919 savanna. *Geophysical Research Letters*, 29, 9–1.

920 Hollmann, R., Merchant, C. J., Saunders, R., Downy, C., Buchwitz, M., Cazenave, A., Chuvieco, E., Defourny, P., de Leeuw, G., Forsberg, R.
921 et al. (2013). The ESA climate change initiative: Satellite data records for essential climate variables. *Bulletin of the American Meteorological
922 Society*, 94, 1541–1552.

923 Hu, Z., Zhou, Q., Chen, X., Li, J., Li, Q., Chen, D., Liu, W., & Yin, G. (2018). Evaluation of three global gridded precipitation data sets in central
924 Asia based on rain gauge observations. *International Journal of Climatology*, 38, 3475–3493.

925 Huang, S., & Siegert, F. (2006). Backscatter change on fire scars in Siberian boreal forests in ENVISAT ASAR wide-swath images. *IEEE
926 Geoscience and Remote Sensing Letters*, 3, 154–158.

927 Humber, M. L., Boschetti, L., Giglio, L., & Justice, C. O. (2018). Spatial and temporal intercomparison of four global burned area products.
928 *International Journal of Digital Earth*, (pp. 1–25).

929 Imperatore, P., Azar, R., Calo, F., Stroppiana, D., Brivio, P. A., Lanari, R., & Pepe, A. (2017). Effect of the Vegetation Fire on Backscattering:
930 An Investigation Based on Sentinel-1 Observations. *IEEE Journal of Selected Topics in Applied Earth Observations and Remote Sensing*, 10,
931 4478–4492.

932 Inglada, J., & Christophe, E. (2009). The Orfeo Toolbox remote sensing image processing software. In *Geoscience and Remote Sensing Symposium,
933 2009 IEEE International, IGARSS 2009* (pp. IV–733). IEEE volume 4.

934 Kalogirou, V., Ferrazzoli, P., Della Vecchia, A., & Fomelis, M. (2014). On the SAR backscatter of burned forests: A model-based study in C-band,
935 over burned pine canopies. *IEEE Transactions on Geoscience and Remote Sensing*, 52, 6205–6215.

936 Kasischke, E. S., Bourgeau-Chavez, L. L., & French, N. H. (1994). Observations of variations in ERS-1 SAR image intensity associated with forest
937 fires in Alaska. *IEEE Transactions on Geoscience and Remote Sensing*, 32, 206–210.

938 Keeley, J. E. (2009). Fire intensity, fire severity and burn severity: a brief review and suggested usage. *International Journal of Wildland Fire*, 18,
939 116–126.

940 Key, C., & Benson, N. (2006). Ground measure of severity, the Composite Burn Index; and Remote sensing of severity, the Normalized Burn Ratio.

941 In G. T. R. RMRS-GTR-164 (Ed.), *FIREMON: Fire Effects Monitoring and Inventory System* chapter Landscape assessment (LA): Sampling
942 and analysis methods. (pp. 1–51). Ogden: USDA Forest Service, Rocky Mountain Research Station.

943 Kirches, G., Brockmann, C., Boettcher, M., Peters, M., Bontemps, S., Lamarche, C., Schlerf, M., Santoro, M., & Defourny, P. (2014). Land Cover
944 CCI-Product User Guide-Version 2. *ESA Public Document CCI-LC-PUG*, (p. 4).

945 Kloster, S., Mahowald, N., Randerson, J., & Lawrence, P. (2012). The impacts of climate, land use, and demography on fires during the 21st
946 century simulated by CLM-CN. *Biogeosciences*, *9*, 509–525.

947 Knorr, W., Jiang, L., & Arneth, A. (2016). Climate, CO₂ and human population impacts on global wildfire emissions. *Biogeosciences*, *13*,
948 267–282.

949 Krawchuk, M. A., Moritz, M. A., Parisien, M.-A., Van Dorn, J., & Hayhoe, K. (2009). Global pyrogeography: the current and future distribution
950 of wildfire. *PLoS one*, *4*, e5102.

951 Kurum, M. (2015). C-band SAR backscatter evaluation of 2008 Gallipoli forest fire. *IEEE Geoscience and Remote Sensing Letters*, *12*, 1091–1095.

952 Kwon, H., & Nasrabadi, N. M. (2005). Kernel RX-algorithm: A nonlinear anomaly detector for hyperspectral imagery. *IEEE Transactions on*
953 *Geoscience and Remote Sensing*, *43*, 388–397.

954 Lacava, T., Coviello, I., Faruolo, M., Mazzeo, G., Pergola, N., & Tramutoli, V. (2013). A multitemporal investigation of AMSR-E C-band radio-
955 frequency interference. *IEEE Transactions on Geoscience and Remote Sensing*, *51*, 2007–2015.

956 Langenfels, R., Francey, R., Pak, B., Steele, L., Lloyd, J., Trudinger, C., & Allison, C. (2002). Interannual growth rate variations of atmospheric
957 CO₂ and its $\delta^{13}C$, H₂, CH₄, and CO between 1992 and 1999 linked to biomass burning. *Global Biogeochemical Cycles*, *16*, 21–1.

958 Lavorel, S., Flannigan, M. D., Lambin, E. F., & Scholes, M. C. (2007). Vulnerability of land systems to fire: Interactions among humans, climate,
959 the atmosphere, and ecosystems. *Mitigation and Adaptation Strategies for Global Change*, *12*, 33–53.

960 Li, L., Njoku, E. G., Im, E., Chang, P. S., & Germain, K. S. (2004). A preliminary survey of radio-frequency interference over the US in Aqua
961 AMSR-E data. *IEEE Transactions on Geoscience and Remote Sensing*, *42*, 380–390.

962 Loboda, T., O'neal, K., & Csiszar, I. (2007). Regionally adaptable dNBR-based algorithm for burned area mapping from MODIS data. *Remote*
963 *Sensing of Environment*, *109*, 429–442.

964 Lohberger, S., Stängel, M., Atwood, E. C., & Siegert, F. (2018). Spatial evaluation of Indonesia's 2015 fire-affected area and estimated carbon
965 emissions using Sentinel-1. *Global change biology*, *24*, 644–654.

966 Meddens, A. J., Kolden, C. A., & Lutz, J. A. (2016). Detecting unburned areas within wildfire perimeters using Landsat and ancillary data across
967 the northwestern United States. *Remote Sensing of Environment*, *186*, 275–285.

968 Menges, C., Bartolo, R., Bell, D., & Hill, G. E. (2004). The effect of savanna fires on SAR backscatter in northern Australia. *International Journal*
969 *of Remote Sensing*, *25*, 4857–4871.

970 Mouillot, F., Schultz, M. G., Yue, C., Cadule, P., Tansey, K., Ciais, P., & Chuvieco, E. (2014). Ten years of global burned area products from
971 spaceborne remote sensing—A review: Analysis of user needs and recommendations for future developments. *International Journal of Applied*
972 *Earth Observation and Geoinformation*, *26*, 64–79.

973 Njoku, E. G., Ashcroft, P., Chan, T. K., & Li, L. (2005). Global survey and statistics of radio-frequency interference in AMSR-E land observations.
974 *IEEE Transactions on Geoscience and Remote Sensing*, *43*, 938–947.

975 Padilla, M., Olofsson, P., Stehman, S. V., Tansey, K., & Chuvieco, E. (2017). Stratification and sample allocation for reference burned area data.
976 *Remote Sensing of Environment*, *203*, 240–255.

977 Padilla, M., Stehman, S. V., & Chuvieco, E. (2014). Validation of the 2008 MODIS-MCD45 global burned area product using stratified random
978 sampling. *Remote Sensing of Environment*, *144*, 187–196.

979 Padilla, M., Stehman, S. V., Ramo, R., Corti, D., Hantson, S., Oliva, P., Alonso-Canas, I., Bradley, A. V., Tansey, K., Mota, B. et al. (2015).
980 Comparing the accuracies of remote sensing global burned area products using stratified random sampling and estimation. *Remote Sensing of*
981 *Environment*, *160*, 114–121.

982 Pal, M. (2005). Random forest classifier for remote sensing classification. *International Journal of Remote Sensing*, *26*, 217–222.

983 Pausas, J. G., & Paula, S. (2012). Fuel shapes the fire–climate relationship: evidence from Mediterranean ecosystems. *Global Ecology and*

984 *Biogeography*, 21, 1074–1082.

985 Pazzani, M., Merz, C., Murphy, P., Ali, K., Hume, T., & Brunk, C. (1994). Reducing misclassification costs. In *Machine Learning Proceedings*
986 *1994* (pp. 217–225).

987 Plummer, S., Arino, O., Simon, M., & Steffen, W. (2006). Establishing a earth observation product service for the terrestrial carbon community:
988 The GLOBCARBON initiative. *Mitigation and Adaptation Strategies for Global Change*, 11, 97–111.

989 Plummer, S., Lecomte, P., & Doherty, M. (2017). The ESA Climate Change Initiative (CCI): A European contribution to the generation of the
990 Global Climate Observing System. *Remote Sensing of Environment*, 203, 2–8.

991 Polychronaki, A., Gitas, I. Z., Veraverbeke, S., & Debien, A. (2013). Evaluation of ALOS PALSAR imagery for burned area mapping in Greece
992 using object-based classification. *Remote Sensing*, 5, 5680–5701.

993 Poulter, B., Cadule, P., Cheiney, A., Ciais, P., Hodson, E., Peylin, P., Plummer, S., Spessa, A., Saatchi, S., Yue, C. et al. (2015). Sensitivity of
994 global terrestrial carbon cycle dynamics to variability in satellite-observed burned area. *Global Biogeochemical Cycles*, 29, 207–222.

995 Quegan, S., Le Toan, T., Yu, J. J., Ribbes, F., & Floury, N. (2000). Multitemporal ERS SAR analysis applied to forest mapping. *IEEE Transactions*
996 *on Geoscience and Remote Sensing*, 38, 741–753.

997 Ramo, R., & Chuvieco, E. (2017). Developing a Random Forest Algorithm for MODIS Global Burned Area Classification. *Remote Sensing*, 9,
998 1193.

999 Randerson, J., Chen, Y., Werf, G., Rogers, B., & Morton, D. (2012). Global burned area and biomass burning emissions from small fires. *Journal*
1000 *of Geophysical Research: Biogeosciences*, 117.

1001 Reed, I. S., & Yu, X. (1990). Adaptive multiple-band CFAR detection of an optical pattern with unknown spectral distribution. *Acoustics, Speech*
1002 *and Signal Processing, IEEE Transactions on*, 38, 1760–1770.

1003 Rignot, E., Despain, D., & Holecz, F. (1999). The 1988 Yellowstone fires observed by imaging radars. In *Proceedings of the Joint Fire Sciences*
1004 *Conference and Workshop*. volume 1.

1005 Rodriguez-Galiano, V. F., Ghimire, B., Rogan, J., Chica-Olmo, M., & Rigol-Sanchez, J. P. (2012). An assessment of the effectiveness of a random
1006 forest classifier for land-cover classification. *ISPRS Journal of Photogrammetry and Remote Sensing*, 67, 93–104.

1007 Roteta, E., Bastarrika, A., Padilla, M., Storm, T., & Chuvieco, E. (2019). Development of a Sentinel-2 burned area algorithm: Generation of a
1008 small fire database for sub-Saharan Africa. *Remote Sensing of Environment*, 222, 1–17.

1009 Roy, D. P., Boschetti, L., Justice, C. O., & Ju, J. (2008). The collection 5 MODIS burned area product—Global evaluation by comparison with the
1010 MODIS active fire product. *Remote Sensing of Environment*, 112, 3690–3707.

1011 Ruecker, G., & Siegert, F. (2000). Burn scar mapping and fire damage assessment using ERS-2 SAR images in East Kalimantan, Indonesia.
1012 *International Archives of Photogrammetry and Remote Sensing*, 33, 1286–1293.

1013 Schroeder, W., Oliva, P., Giglio, L., & Csiszar, I. A. (2014). The New VIIRS 375 m active fire detection data product: Algorithm description and
1014 initial assessment. *Remote Sensing of Environment*, 143, 85–96.

1015 Siegert, F., & Hoffmann, A. A. (2000). The 1998 forest fires in East Kalimantan (Indonesia): A quantitative evaluation using high resolution,
1016 multitemporal ERS-2 SAR images and NOAA-AVHRR hotspot data. *Remote Sensing of Environment*, 72, 64–77.

1017 Siegert, F., & Ruecker, G. (2000). Use of multitemporal ERS-2 SAR images for identification of burned scars in south-east Asian tropical rainforest.
1018 *International Journal of Remote Sensing*, 21, 831–837.

1019 Simon, M., Plummer, S., Fierens, F., Hoelzemann, J. J., & Arino, O. (2004). Burnt area detection at global scale using ATSR-2: The GLOBSCAR
1020 products and their qualification. *Journal of Geophysical Research: Atmospheres*, 109.

1021 Small, D. (2011). Flattening gamma: Radiometric terrain correction for SAR imagery. *IEEE Transactions on Geoscience and Remote Sensing*, 49,
1022 3081–3093.

1023 Stein, D. W., Beaven, S. G., Hoff, L. E., Winter, E. M., Schaum, A. P., & Stocker, A. D. (2002). Anomaly detection from hyperspectral imagery.
1024 *IEEE Signal Processing Magazine*, 19, 58–69.

1025 Stroppiana, D., Azar, R., Calò, F., Pepe, A., Imperatore, P., Boschetti, M., Silva, J., Brivio, P. A., & Lanari, R. (2015a). Integration of optical and
1026 SAR data for burned area mapping in Mediterranean Regions. *Remote Sensing*, 7, 1320–1345.

- 1027 Stroppiana, D., Azar, R., Calò, F., Pepe, A., Imperatore, P., Boschetti, M., Silva, J. M., Brivio, P. A., & Lanari, R. (2015b). Remote sensing of
1028 burned area: A fuzzy-based framework for joint processing of optical and microwave data. In *Geoscience and Remote Sensing Symposium*
1029 *(IGARSS), 2015 IEEE International* (pp. 1409–1412). IEEE.
- 1030 Tanase, M., Kennedy, R., & Aponte, C. (2015). Radar Burn Ratio for fire severity estimation at canopy level: An example for temperate forests.
1031 *Remote Sensing of Environment, 170*, 14–31.
- 1032 Tanase, M., de la Riva, J., & Pérez-Cabello, F. (2011). Estimating burn severity at the regional level using optically based indices. *Canadian*
1033 *Journal of Forest Research, 41*, 863–872.
- 1034 Tanase, M., Santoro, M., de la Riva, J., & Pérez-Cabello, F. (2009). Backscatter properties of multitemporal TerraSAR-X data and the effects
1035 of influencing factors on burn severity evaluation, in a Mediterranean pine forest. In *Geoscience and Remote Sensing Symposium, 2009 IEEE*
1036 *International, IGARSS 2009* (pp. III–593). IEEE volume 3.
- 1037 Tanase, M. A., Aponte, C., Mermoz, S., Bouvet, A., Le Toan, T., & Heurich, M. (2018). Detection of windthrows and insect outbreaks by L-band
1038 SAR: A case study in the Bavarian Forest National Park. *Remote Sensing of Environment, 209*, 700–711.
- 1039 Tanase, M. A., & Belenguer-Plomer, M. A. (2018). 03. D3 Intermediate validation results: SAR pre-processing and burned area detection, version
1040 1.0. ESA Climate Change Initiative–Fire_cci.
- 1041 Tanase, M. A., Perez-Cabello, F., de La Riva, J., & Santoro, M. (2010a). TerraSAR-X data for burn severity evaluation in Mediterranean forests on
1042 sloped terrain. *IEEE Transactions on Geoscience and Remote Sensing, 48*, 917–929.
- 1043 Tanase, M. A., Santoro, M., Aponte, C., & de la Riva, J. (2014). Polarimetric properties of burned forest areas at C-and L-band. *IEEE Journal of*
1044 *Selected Topics in Applied Earth Observations and Remote Sensing, 7*, 267–276.
- 1045 Tanase, M. A., Santoro, M., de La Riva, J., Fernando, P., Le Toan, T. et al. (2010b). Sensitivity of X-, C-, and L-band SAR backscatter to burn
1046 severity in Mediterranean pine forests. *IEEE Transactions on Geoscience and Remote Sensing, 48*, 3663–3675.
- 1047 Tanase, M. A., Santoro, M., Wegmüller, U., de la Riva, J., & Pérez-Cabello, F. (2010c). Properties of X-, C-and L-band repeat-pass interferometric
1048 SAR coherence in Mediterranean pine forests affected by fires. *Remote Sensing of Environment, 114*, 2182–2194.
- 1049 Tansey, K., Grégoire, J.-M., Defourny, P., Leigh, R., Pekel, J.-F., van Bogaert, E., & Bartholomé, E. (2008). A new, global, multi-annual (2000–
1050 2007) burnt area product at 1 km resolution. *Geophysical Research Letters, 35*.
- 1051 Tansey, K., Grégoire, J.-M., Stroppiana, D., Sousa, A., Silva, J., Pereira, J., Boschetti, L., Maggi, M., Brivio, P. A., Fraser, R. et al. (2004). Vegeta-
1052 tion burning in the year 2000: Global burned area estimates from SPOT VEGETATION data. *Journal of Geophysical Research: Atmospheres,*
1053 *109*.
- 1054 Theiler, J., & Perkins, S. (2006). Proposed framework for anomalous change detection. In *ICML Workshop on Machine Learning Algorithms for*
1055 *Surveillance and Event Detection* (pp. 7–14).
- 1056 Van Der Werf, G. R., Randerson, J. T., Giglio, L., Van Leeuwen, T. T., Chen, Y., Rogers, B. M., Mu, M., Van Marle, M. J., Morton, D. C., Collatz,
1057 G. J. et al. (2017). Global fire emissions estimates during 1997-2016. *Earth System Science Data, 9*, 697–720.
- 1058 Van Wagendonk, J. W., Root, R. R., & Key, C. H. (2004). Comparison of AVIRIS and Landsat ETM+ detection capabilities for burn severity.
1059 *Remote Sensing of Environment, 92*, 397–408.
- 1060 Van Zyl, J. J. (1993). The effect of topography on radar scattering from vegetated areas. *IEEE Transactions on Geoscience and Remote Sensing,*
1061 *31*, 153–160.
- 1062 Van Zyl, J. J., Aari, M., & Kim, Y. (2011). Model-based decomposition of polarimetric SAR covariance matrices constrained for nonnegative
1063 eigenvalues. *IEEE Transactions on Geoscience and Remote Sensing, 49*, 3452–3459.
- 1064 Verhegghen, A., Eva, H., Ceccherini, G., Achard, F., Gond, V., Gourlet-Fleury, S., & Cerutti, P. O. (2016). The potential of Sentinel satellites for
1065 burnt area mapping and monitoring in the Congo Basin forests. *Remote Sensing, 8*, 986.
- 1066 Vermote, E., Justice, C., Claverie, M., & Franch, B. (2016). Preliminary analysis of the performance of the Landsat 8/OLI land surface reflectance
1067 product. *Remote Sensing of Environment, 185*, 46–56.
- 1068 Waske, B., & Braun, M. (2009). Classifier ensembles for land cover mapping using multitemporal SAR imagery. *ISPRS Journal of Photogrammetry*
1069 *and Remote Sensing, 64*, 450–457.

- 1070 Watanabe, M., Koyama, C. N., Hayashi, M., Nagatani, I., & Shimada, M. (2018). Early-Stage Deforestation Detection in the Tropics With L-band
1071 SAR. *IEEE Journal of Selected Topics in Applied Earth Observations and Remote Sensing*, *11*, 2127–2133.
- 1072 Van der Werf, G. R., Randerson, J. T., Giglio, L., Collatz, G., Mu, M., Kasibhatla, P. S., Morton, D. C., DeFries, R., Jin, Y. v., & van Leeuwen,
1073 T. T. (2010). Global fire emissions and the contribution of deforestation, savanna, forest, agricultural, and peat fires (1997–2009). *Atmospheric*
1074 *Chemistry and Physics*, *10*, 11707–11735.
- 1075 Xu, S., Qi, Z., Li, X., & Yeh, A. G.-O. (2019). Investigation of the effect of the incidence angle on land cover classification using fully polarimetric
1076 SAR images. *International Journal of Remote Sensing*, *40*, 1576–1593.
- 1077 Yamaguchi, Y., Moriyama, T., Ishido, M., & Yamada, H. (2005). Four-component scattering model for polarimetric SAR image decomposition.
1078 *IEEE Transactions on Geoscience and Remote Sensing*, *43*, 1699–1706.

1079 **List of Figure Captions**

1080 Fig. 1 Location of the Military Grid Reference System tiles used for algorithm development and valida-
 1081 tion. 5

1082 Fig. 2 SAR data processing with the Orfeo Toolbox. 6

1083 Fig. 3 Flowchart of the SAR based algorithm for burned area detection. 9

1084 Fig. 4 Graphical representation of concepts needed to extract bROIs, being HS - hotspot. 11

1085 Fig. 5 Maps of burned area detected using Sentinel-1 data per MGRS tiles. Errors of omission and
 1086 commission are also shown. 19

1087 Fig. 6 Assessment metrics of Sentinel-1 and MCD64A1 Version 6 burned area detections per MGRS
 1088 tiles and land cover classes. The metrics by land cover were computed using confusion matrices
 1089 formed by pixels of the same land cover class from all tiles. DC - Dice coefficient, OE - omission
 1090 error and CE - commission error. 20

1091 Fig. 7 Dispersion of Dice coefficient (DC), omission and commission errors (OE and CE) of burned
 1092 area detected for all tiles for Sentinel-1 (S1) and MCD64A1 Version 6. The red line indicates median
 1093 value, and top and bottom box edges indicate the 75th and 25th percentiles, respectively, while red
 1094 dots indicate outliers. 21

1095 Fig. 8 Temporal variation ($\Delta = data_{pre} - data_{post}$) of the backscatter coefficient (dB) and soil moisture
 1096 (from SMAP) between pre- and post-dates for BA detection periods. MAC values from RXD are also
 1097 presented. Values are displayed by land cover classes for four categories of pixels: unburned (Un),
 1098 burned (Bu) and commission (Ce) and omission errors (Oe). Red line indicates median value. Top
 1099 and bottom box edges indicate the 75th and respectively the 25th percentiles. Outliers not shown to
 1100 improved graphs discernibility. 23

1101 Fig. 9 Assessment metrics of Sentinel-1 burned area detections per ascending (A), descending (D) and
 1102 both satellite passes (B). DC - Dice coefficient, OE - omission error and CE - commission error. . . . 25

1103 Fig. 10 Dice coefficient (DC) by local incidence angle (LIA) and local slope (U) groups. For sloped
 1104 areas ($U \geq 5^\circ$ degrees) the DC, commission (CE) and omission errors (OE) are shown as a function
 1105 of slope orientation (V) with respect to the Sentinel-1 viewing geometry. Negative V values show
 1106 slopes oriented away the sensor while positive V values show slopes oriented toward the sensor. The
 1107 BA metrics are shown for six tiles where both ascending (ASC) and descending (DESC) passes were
 1108 available (i.e., 10SEH, 10UEC, 29TNE, 29TNG, 30SVG and 30TYK). 26

1109 Fig. 11 Temporal variations of soil moisture (SM) from Soil Moisture Active Passive (SMAP) mission
 1110 for pre- and post-fire dates ($\Delta_{SM} = SM_{pre} - SM_{post}$), in tile 30SVG. Ascending (A) and descending
 1111 (D) passes are analyzed separately. Pixels are grouped by classes of unburned (Un) and burned (Bu).
 1112 Pixels from areas affected by commission (Ce) and omission errors (Oe) are also shown. The red
 1113 line indicates median value, and top and bottom box edges indicate the 75th and respectively the 25th
 1114 percentiles. Outliers are not shown to improve graph discernibility. 27

1115 Fig. 12 Burned area from ascending (left column) and descending (right column) passes in tile 30SVG:
 1116 red – burned (Bu), white – unburned (Un), black – omission errors (Oe) and blue – commission errors
 1117 (Ce). VV and VH backscatter coefficient variation ($\Delta\gamma^0 = pre_{fire} - post_{fire}$) is also shown for each
 1118 pass. 28